PLOS GENETICS

RESEARCH ARTICLE

Dual function of perivascular fibroblasts in vascular stabilization in zebrafish

Arsheen M. Rajan[1], Roger C. Ma[1], Katrinka M. Kocha[1], Dan J. Zhang[2], Peng Huang[1]*

1 Department of Biochemistry and Molecular Biology, Cumming School of Medicine, Alberta Children's Hospital Research Institute, University of Calgary, Calgary, Alberta, Canada, **2** Department of Biological Sciences, University of Calgary, Calgary, Alberta, Canada

* huangp@ucalgary.ca

Check for updates

OPEN ACCESS

Citation: Rajan AM, Ma RC, Kocha KM, Zhang DJ, Huang P (2020) Dual function of perivascular fibroblasts in vascular stabilization in zebrafish. PLoS Genet 16(10): e1008800. https://doi.org/10.1371/journal.pgen.1008800

Editor: Mary C. Mullins, University of Pennsylvania School of Medicine, UNITED STATES

Received: April 21, 2020

Accepted: September 28, 2020

Published: October 26, 2020

Data Availability Statement: All relevant data are within the manuscript and its Supporting Information files.

Funding: This study was supported by grants to PH from the Canadian Institute of Health Research (MOP-136926 and PJT-169113, https://cihr-irsc.gc.ca/e/193.html), Canada Foundation for Innovation John R. Evans Leaders Fund (Project 32920, https://www.innovation.ca/), and Startup Fund from the Alberta Children's Hospital Research Institute (ACHRI, https://research4kids.ucalgary.ca/). The funders had no role in study design, data

Abstract

Blood vessels are vital to sustain life in all vertebrates. While it is known that mural cells (pericytes and smooth muscle cells) regulate vascular integrity, the contribution of other cell types to vascular stabilization has been largely unexplored. Using zebrafish, we identified sclerotome-derived perivascular fibroblasts as a novel population of blood vessel associated cells. In contrast to pericytes, perivascular fibroblasts emerge early during development, express the extracellular matrix (ECM) genes *col1a2* and *col5a1*, and display distinct morphology and distribution. Time-lapse imaging reveals that perivascular fibroblasts serve as pericyte precursors. Genetic ablation of perivascular fibroblasts markedly reduces collagen deposition around endothelial cells, resulting in dysmorphic blood vessels with variable diameters. Strikingly, *col5a1* mutants show spontaneous hemorrhage, and the penetrance of the phenotype is strongly enhanced by the additional loss of *col1a2*. Together, our work reveals dual roles of perivascular fibroblasts in vascular stabilization where they establish the ECM around nascent vessels and function as pericyte progenitors.

Author summary

Blood vessels are essential to sustain life in humans. Defects in blood vessels can lead to serious diseases, such as hemorrhage, tissue ischemia, and stroke. However, how blood vessel stability is maintained by surrounding support cells is still poorly understood. Using the zebrafish model, we identify a new population of blood vessel associated cells termed perivascular fibroblasts, which originate from the sclerotome, an embryonic structure that is previously known to generate the skeleton of the animal. Perivascular fibroblasts are distinct from pericytes, a known population of blood vessel support cells. They become associated with blood vessels much earlier than pericytes and express several collagen genes, encoding main components of the extracellular matrix. Loss of perivascular fibroblasts or mutations in collagen genes result in fragile blood vessels prone to damage. Using cell tracing in live animals, we find that a subset of perivascular fibroblasts can differentiate into pericytes. Together, our work shows that perivascular fibroblasts play two important roles in maintaining blood vessel integrity. Perivascular fibroblasts

collection and analysis, decision to publish, or preparation of the manuscript.

Competing interests: The authors have declared that no competing interests exist.

secrete collagens to stabilize newly formed blood vessels and a sub-population of these cells also functions as precursors to generate pericytes to provide additional vascular support.

Introduction

The vascular system is crucial to the survival of vertebrates. Blood vessels must rapidly expand and contract in response to systemic cues, but also be sturdy to withstand the stress of blood flow. To maintain their integrity, blood vessels are supported by a highly specialized perivascular architecture comprised of blood vessel associated cells and the surrounding extracellular matrix (ECM) [1, 2]. Compromised vascular integrity can result in devastating human diseases, such as aneurysms, vascular malformations, and hemorrhagic strokes [3–6]. However, how blood vessels are stabilized by different perivascular components is still poorly understood.

The prevailing model is that vascular stability is maintained at three different levels: endothelial cells, mural cells and the surrounding ECM [2]. First, blood vessels are lined by endothelial cells. Adherens and tight junctions between endothelial cells provide the primary barrier to passage of fluids, cells, and macromolecules between blood and tissues [7]. Second, vascular smooth muscle cells (vSMCs) and pericytes, collectively known as mural cells, closely interact with and stabilize the endothelium [8]. vSMCs form a continuous protective sheath around large diameter blood vessels, whereas pericytes are solitary cells partially covering smaller blood vessels such as capillaries. Defects in mural cell specification or recruitment result in widespread vascular leakage and early lethality in mice [9–13]. Lastly, the vascular ECM provides structural support for blood vessels [1, 14]. Mutations in ECM proteins, such as collagens and laminins, lead to early death due to blood vessel rupture in mice [15–18]. In humans, defects in fibril forming collagens (type I, III and V), as well as molecules involved in collagen modification and processing, have been associated with Ehlers-Danlos syndrome (EDS) [19]. EDS patients are characterized by a significant vascular fragility that often leads to spontaneous rupture of blood vessel walls. Thus, work in both animal models and human patients shows the importance of collagen in maintaining vascular stability. However, one unresolved question is how newly formed blood vessels are stabilized in the early time window before the differentiation of mural cells.

vSMCs and pericytes are the most well-studied blood vessel associated cells and are classically defined by the expression of alpha smooth muscle actin (ACTA2) and platelet-derived growth factor receptor b (PDGFRb), respectively [20, 21]. Lineage tracing in mice and chick-quail chimeras demonstrate a heterogeneous developmental origin of mural cells [20–23]. For example, vSMCs covering the trunk aorta originate from either the neural crest or the sclerotome of the somite, depending on the axial position. Other than mural cells, several types of perivascular cells have been identified, including adventitial cells [24], fibroblasts [25], immune cells [26], and astrocytes [27]. However, whether these different cell types play roles in vascular stabilization is unknown.

Recent single cell transcriptional profiling studies in mice have revealed the presence of perivascular fibroblast-like cells in the adult mouse brain that are not labeled by classical mural cell markers [28–31]. In contrast to mural cells, perivascular fibroblast-like cells adhere loosely to blood vessels and show robust expression of many ECM components, such as collagens. Previous studies have described similar cell populations in the mouse central nervous system that contribute to fibrotic scar formation after injury [32–35]. However, where these perivascular fibroblast-like cells originate from during development and how they regulate blood vessel development and stabilization have not been explored.

Zebrafish is a powerful model to study human cardiovascular diseases [36–38]. The organization, development and function of the vasculature, including mural cells, are highly conserved between zebrafish and mammals [36, 39–41]. In the zebrafish trunk, intersegmental vessels (ISVs) sprout from the dorsal aorta (DA) at around 24 hpf (hours post fertilization) and fully establish the metameric pattern by 36 hpf [42]. Interestingly, pericytes, the primary mural cells along the ISVs, only emerge at 60 hpf [43]. This raises the question how nascent blood vessels are stabilized prior to the differentiation of pericytes. In our work, we describe a novel population of collagen-expressing perivascular fibroblasts that become closely associated with ISVs soon after vessel formation. Perivascular fibroblasts originate from the sclerotome and are distinct from pericytes in their morphology, distribution, and marker expression. Using a combination of *in vivo* live imaging, genetic ablation and CRISPR mutant analysis, we demonstrate that perivascular fibroblasts play dual roles in stabilizing nascent ISVs by regulating the vascular ECM and later functioning as pericyte progenitors. Together, our work provides important insights into the development of perivascular support structures and suggests a molecular and cellular basis of Ehlers-Danlos syndrome.

Results

Perivascular fibroblasts express several collagen genes

We previously developed a sclerotome-specific transgenic line *nkx3.1*:*Gal4; UAS*:*Nitroreductase-mCherry* (*nkx3.1*$^{NTR\text{-}mCherry}$, similar designations are used for all Gal4/UAS transgenic lines in this paper) [44]. This reporter labels the initial sclerotome domains as well as their descendants due to the perdurance of the mCherry protein. Examination of the *nkx3.1*$^{NTR\text{-}mCherry}$ line in combination with an endothelial reporter, *kdrl*:*EGFP*, revealed that a population of mCherry$^+$ cells was closely associated with intersegmental vessels (ISVs) at 48 hpf (Fig 1A). This result suggests that the sclerotome contributes to a population of perivascular cells well before the appearance of pericytes at 60 hpf [43]. Interestingly, *nkx3.1*$^{NTR\text{-}mCherry}$-expressing perivascular cells at 52 hpf were also labeled by a pan-fibroblast reporter, *col1a2*:*GFP* [44] (Fig 1B). On average, 37% of mCherry$^+$ perivascular cells were positive for *col1a2*:*GFP* (S1A Fig), which likely reflects the mosaic nature of the *col1a2*:*GFP* line. Consistent with this result, fluorescent in situ hybridization showed that ISV-associated perivascular cells co-expressed several ECM genes, including *col1a2* (*collagen 1a2*) and *col5a1* (*collagen 5a1*) at 48 hpf (Figs 1C and S1B). These collagen-expressing perivascular cells are reminiscent of perivascular fibroblast-like cells recently identified in the adult mouse brain by single cell RNA sequencing [28–31]. We therefore refer to this population of collagen-expressing ISV-associated cells as 'perivascular fibroblasts'.

Perivascular fibroblasts originate from the sclerotome

The expression of *nkx3.1*$^{NTR\text{-}mCherry}$ in perivascular fibroblasts suggests that the sclerotome is the embryonic source of these cells. We have previously shown that the sclerotome in zebrafish has a bipartite organization with a ventral domain and a smaller dorsal domain [44]. The ventral sclerotome domain further gives rise to a population of notochord associated cells. At 24 hpf, the sclerotome consists of three compartments: the dorsal sclerotome domain, the ventral sclerotome domain, and notochord associated cells derived from the ventral domain (Fig 2A). To determine the contribution of these three compartments to perivascular fibroblasts, we performed confocal time-lapse imaging in *nkx3.1*$^{NTR\text{-}mCherry}$; *kdrl*:*EGFP* embryos. The *nkx3.1*$^{NTR\text{-}mCherry}$ reporter labels sclerotome progenitors and their progeny, while the endothelial specific

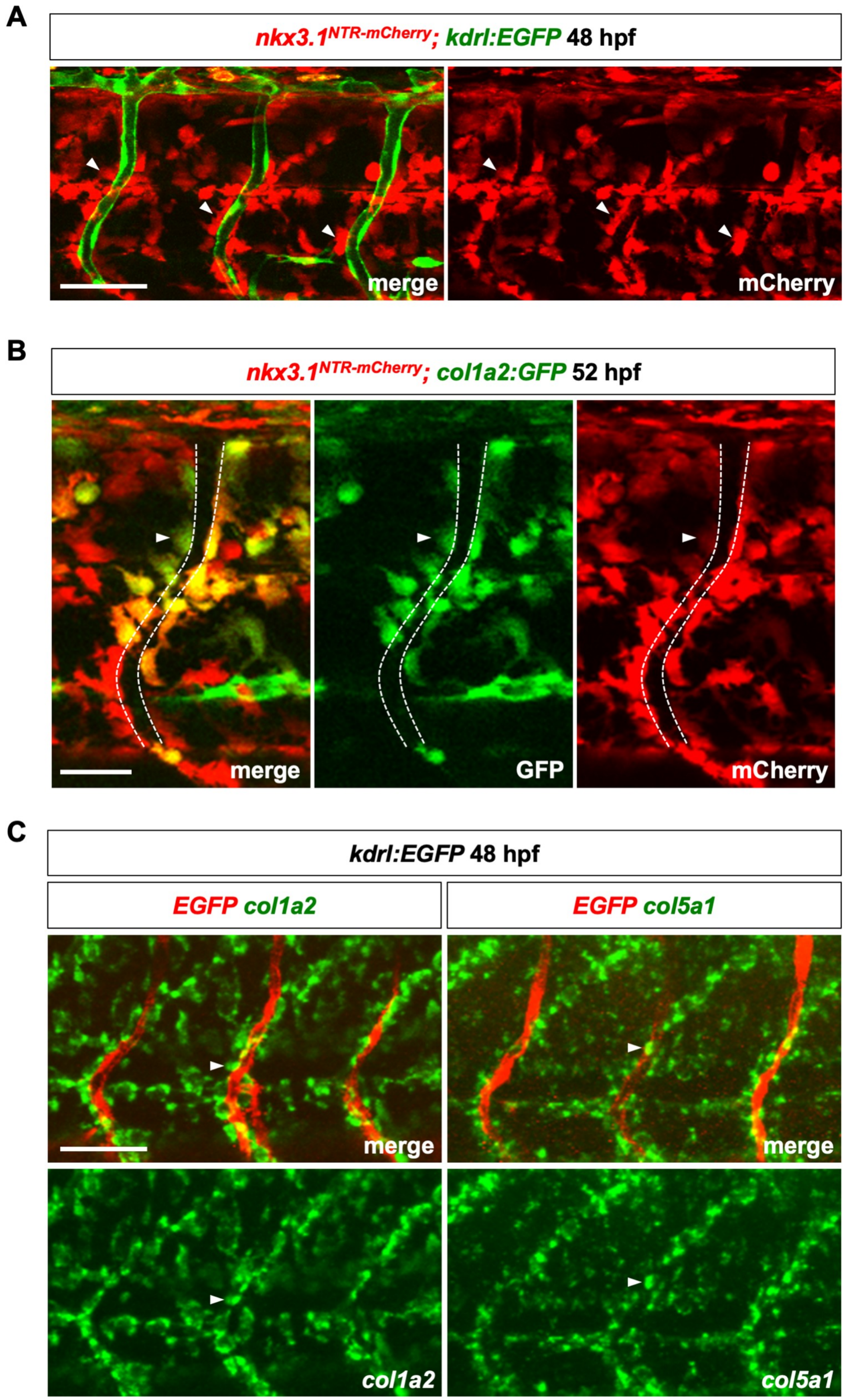
A
nkx3.1NTR-mCherry; kdrl:EGFP 48 hpf
merge
mCherry
B
nkx3.1NTR-mCherry; col1a2:GFP 52 hpf
merge
GFP
mCherry
C
kdrl:EGFP 48 hpf
EGFP col1a2
EGFP col5a1
merge
merge
col1a2
col5a1

Fig 1. Characterization of perivascular fibroblasts in zebrafish. (A) Lateral view of a three somite region in *nkx3.1*$^{NTR\text{-}mCherry}$; *kdrl*:*EGFP* embryos at 48 hpf. Many mCherry$^+$ perivascular fibroblasts (red, arrowheads) were closely associated with intersegmental vessels (ISVs) labeled by the endothelial marker *kdrl*:*EGFP* (green). *n* = 11 embryos. (B) Co-expression of *nkx3.1*$^{NTR\text{-}mCherry}$ and *col1a2*:*GFP* in perivascular fibroblasts (arrowheads) at 52 hpf. The ISV is indicated by dashed lines. Graph showing proportion of perivascular fibroblasts labeled by *col1a2*:*GFP* is shown in S1A Fig. *n* = 17 embryos. (C) Fluorescent mRNA in situ hybridization showing expression of fibrillar collagens *col1a2* (green, left) and *col5a1* (green, right) in perivascular fibroblasts (arrowheads) along ISVs marked by *kdrl*:*EGFP* (red) at 48 hpf. *n* = 15 embryos per staining. Scale bars: (A,C) 50 μm; (B) 25 μm.

https://doi.org/10.1371/journal.pgen.1008800.g001

kdrl:*EGFP* line allows us to visualize the ISVs. Perivascular fibroblasts can be distinguished from tenocytes based on their perivascular locations as well as the lack of long tree-like processes extending into the intersomitic space, a characteristic unique to tenocytes [44]. The trunk region of embryos (somite 12–18) was imaged laterally at 6–9 minute intervals starting at 25 hpf, immediately after the emergence of ISV sprouts (Fig 2B and S1 Video). At 30 hpf, most ISVs became visibly lumenized. During ISV sprouting and lumenization, mCherry$^+$ cells can be observed associated with the *kdrl*:*EGFP*-labeled endothelium (Figs 2B and S2A; S1 Video). By the end of the movie at 49.5 hpf, mCherry$^+$ perivascular fibroblasts 'decorated' the entire ISVs along the dorsal-ventral (D-V) axis. Interestingly, in the absence of ISVs, numerous mCherry$^+$ sclerotome derived cells can still populate the interstitial space between muscles, the spinal cord and the notochord (S2B Fig), suggesting that the migration and proliferation of sclerotome progenitors and their descendants are independent of the vasculature. By retrospective cell tracing, we showed that perivascular fibroblasts can be traced to all three compartments of the sclerotome. Of 170 perivascular fibroblasts traced, 28 cells originated from the dorsal sclerotome domain (16%), 112 from the ventral sclerotome domain (66%), and 30 from notochord associated cells (18%). Since notochord associated cells are derived from the ventral sclerotome domain, this result suggests that the ventral sclerotome is the main contributor of perivascular fibroblasts (142/170 cells, 84%).

To better compare the contribution of sclerotome progenitors from different compartments, we subdivided perivascular fibroblasts into two domains based on their final D-V positions along the ISVs. The position of the horizontal myoseptum was used as a landmark to define perivascular fibroblasts at dorsal or ventral ISVs (Fig 2A). The 170 perivascular fibroblasts can be traced back to 122 sclerotome progenitors. These sclerotome progenitors typically underwent 1–2 cell divisions over the 24-hour period to give rise to multiple daughter cells, at least one of which became associated with the neighboring ISV. We categorized sclerotome progenitors into three groups based on the final positions of perivascular fibroblasts they generated: 1) only at the dorsal ISV, 2) only at the ventral ISV, or 3) at both dorsal and ventral ISV (Fig 2C). Sclerotome progenitors in the dorsal domain gave rise to exclusively perivascular fibroblasts along dorsal ISVs (20/20 cells, 100%) (Fig 2C). Similarly, the majority of sclerotome progenitors around the notochord (i.e., sclerotome derived notochord associated cells) (21/23 cells, 91%) contributed to only perivascular fibroblasts at the dorsal ISV (Fig 2C). By contrast, 48% of sclerotome progenitors in the ventral domain (38/79 cells) gave rise to only perivascular fibroblasts at the ventral ISV, 35% of ventral sclerotome progenitors (28/79 cells) generated only dorsal perivascular fibroblasts, while the remaining 16% of ventral progenitors (13/79 cells) contributed to perivascular fibroblasts at both dorsal and ventral ISV regions (Fig 2C). Similar to the contribution of tendon fibroblasts (tenocytes) [44], the dorsal sclerotome generates only dorsally positioned perivascular fibroblasts, whereas the ventral sclerotome contributes to perivascular fibroblasts along the entire D-V axis of ISVs (the combined bar in Fig 2C). Moreover, perivascular fibroblasts along a given ISV were always derived from the sclerotome of the same overlying somite (170/170 cells, 100%). Together, our results demonstrate that

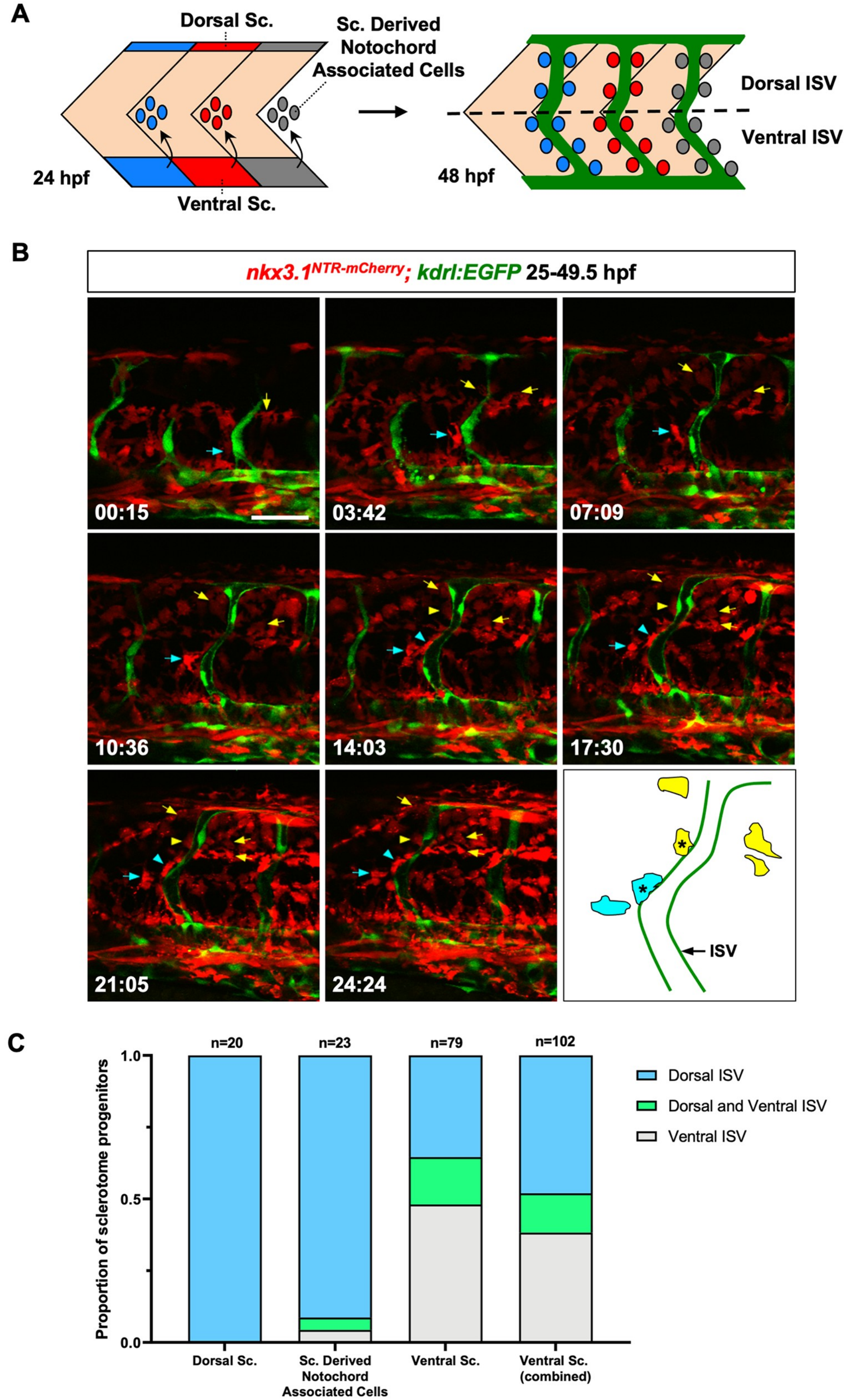
A
Dorsal Sc.
Sc. Derived
Notochord
Associated Cells
24 hpf
Ventral Sc.
48 hpf
Dorsal ISV
Ventral ISV
B
nkx3.1NTR-mCherry; kdrl:EGFP 25-49.5 hpf
00:15
03:42
07:09
10:36
14:03
17:30
21:05
24:24
ISV
C
Proportion of sclerotome progenitors
n=20
n=23
n=79
n=102
1.0
0.5
0.0
Dorsal Sc.
Sc. Derived Notochord Associated Cells
Ventral Sc.
Ventral Sc. (combined)
Dorsal ISV
Dorsal and Ventral ISV
Ventral ISV

Fig 2. Generation of perivascular fibroblasts from different sclerotome domains. (A) Schematic representation of the bipartite organization of the zebrafish sclerotome and the generation of perivascular fibroblasts. At 24 hpf, the zebrafish sclerotome in each somite is divided into three compartments: the dorsal sclerotome, the ventral sclerotome, and sclerotome derived notochord associated cells. Note that notochord associated cells originate from the ventral sclerotome and are located about half-somite posterior to the corresponding somite. At 48 hpf, perivascular fibroblasts appear along the length of the intersegmental vessels (ISVs, green). The dotted line indicates the position of the horizontal myoseptum, which divides any given ISV into a dorsal half and a ventral half. Perivascular fibroblasts were quantified based on their final locations along each ISV: dorsal ISV (above the horizontal myoseptum) or ventral ISV (below the horizontal myoseptum). Sc: sclerotome. (B) Snapshots from time-lapse imaging of a *nkx3.1*$^{NTR\text{-}mCherry}$; *kdrl*:*EGFP* embryo from 25 hpf to 49.5 hpf. Perivascular fibroblasts along ISVs were retrospectively traced to determine their cell of origin. One cell from the ventral sclerotome domain (cyan arrows) and one cell from sclerotome derived notochord associated cells (yellow arrows) were traced over 24.5 hours with their daughter cells indicated by the same colored arrows/arrowheads. Both sclerotome progenitors divided at least once to give rise to one perivascular fibroblast (arrowheads) as well as several interstitial cells (arrows). A schematic representation of color-coded traced cells at the last time point is shown with perivascular fibroblasts indicated by asterisks. The corresponding time-lapse movie is shown in S1 Video. *n* = 6 embryos. (C) Quantification of the contribution of each sclerotome domain to perivascular fibroblasts. Sclerotome progenitors from each domain were quantified based on the final dorsoventral location of perivascular fibroblasts along each ISV. A given sclerotome progenitor can give rise to perivascular fibroblasts in only dorsal ISV, in only ventral ISV, or in both dorsal and ventral ISV as indicated in (A). The ventral sclerotome (combined) group includes progenitors from both the ventral sclerotome domain and sclerotome derived notochord associated cells. *n* = 122 sclerotome progenitors from 6 embryos. Scale bar: 50 μm.

https://doi.org/10.1371/journal.pgen.1008800.g002

perivascular fibroblasts originate from all three sclerotome compartments in a stereotypic manner.

Perivascular fibroblasts are distinct from pericytes

Mural cells, including pericytes and vSMCs, are known blood vessel associated support cells. We next asked whether perivascular fibroblasts represent a different perivascular cell population from mural cells. In the zebrafish trunk, pericytes are associated with ISVs, while vSMCs are localized to larger vessels such as the dorsal aorta [40, 41, 43]. Platelet derived growth factor (PDGF) signaling is known to play an important role in pericyte recruitment and the platelet derived growth factor receptor-beta (*pdgfrb)* is a well-established pericyte marker [43, 45, 46]. We utilized the *pdgfrb*:*GFP* [47] and *pdgfrb*:*Gal4FF; UAS*:*NTR-mCherry* (referred to as *pdgfrb*$^{NTR\text{-}mCherry}$) [48] lines to label pericytes. Interestingly, while both *pdgfrb*:*GFP* and *pdgfrb*$^{NTR\text{-}mCherry}$ lines labeled pericytes (GFP^{high}mCherry^{+} expression) at 4 dpf, *pdgfrb*:*GFP* but not *pdgfrb*$^{NTR\text{-}mCherry}$ also marked perivascular fibroblasts (GFP^{low}mCherry^{-} expression) at 2 and 4 dpf (days post fertilization) (S3A and S3B Fig). Fully differentiated pericytes can be reliably identified based on their elevated *pdgfrb*:*GFP* expression (2.5 fold) compared to perivascular fibroblasts (S3C Fig). The expression of *pdgfrb*:*GFP* in sclerotome descendants is consistent with the previous report that the sclerotome expresses *pdgfrb* [49], suggesting that *pdgfrb*:*GFP* is a more sensitive reporter than the *pdgfrb*$^{NTR\text{-}mCherry}$ line. Indeed, *pdgfrb*$^{NTR\text{-}mCherry}$ labeled about 62% of *pdgfrb*:*GFP*-positive pericytes at 4 dpf (S3D Fig).

Using the two *pdgfrb* lines for pericytes as well as the *nkx3.1*$^{NTR\text{-}mCherry}$ and *col1a2*:*GFP* reporters for perivascular fibroblasts, we found that perivascular fibroblasts and pericytes represent distinct cell populations. First, they showed different developmental timing and cell numbers. Consistent with our time-lapse movies, *nkx3.1*$^{NTR\text{-}mCherry}$-positive perivascular fibroblasts were present along ISVs at 2 dpf (Fig 3A). They were equally distributed along arterial and venous ISVs, and remained largely constant in number (ranging from 9.7 to 10.6 per ISV) from 2 to 4 dpf (Fig 3A). By contrast, pericytes marked by high level of *pdgfrb*:*GFP* expression did not appear on ISVs until 3 dpf. They were more concentrated along arterial ISVs than venous ISVs, and increased in cell number to 2.2 per aISV and 1.0 per vISV by 4 dpf (Fig 3A), similar to what has been previously described [43]. Second, perivascular fibroblasts and pericytes showed distinct marker expression (Fig 3B). Perivascular fibroblasts labeled by *col1a2*:

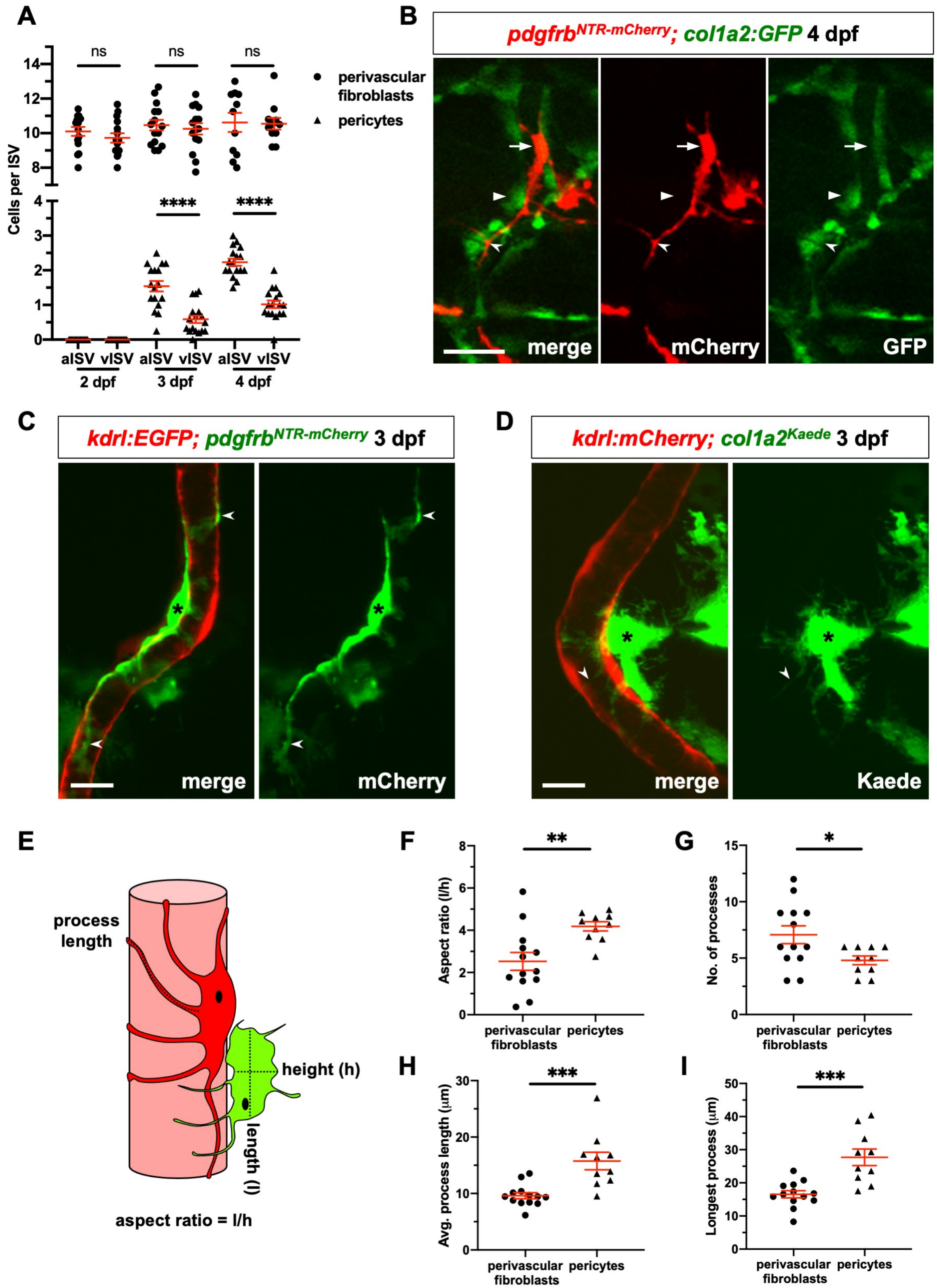
A
ns
ns
ns
perivascular fibroblasts
pericytes
Cells per ISV
****
****
aISV vISV aISV vISV aISV vISV
2 dpf
3 dpf
4 dpf
B
pdgfrbNTR-mCherry; col1a2:GFP 4 dpf
merge
mCherry
GFP
C
kdrl:EGFP; pdgfrbNTR-mCherry 3 dpf
merge
mCherry
D
kdrl:mCherry; col1a2Kaede 3 dpf
merge
Kaede
E
process length
height (h)
length (l)
aspect ratio = l/h
F
Aspect ratio (l/h)
**
perivascular fibroblasts
pericytes
G
No. of processes
*
perivascular fibroblasts
pericytes
H
Avg. process length (μm)
***
perivascular fibroblasts
pericytes
I
Longest process (μm)
***
perivascular fibroblasts
pericytes

Fig 3. Perivascular fibroblasts are distinct from pericytes. (A) Quantification of perivascular cell numbers along arterial ISVs (aISVs) and venous ISVs (vISVs) at 2, 3, and 4 dpf. The number of perivascular fibroblasts and pericytes were scored in *nkx3.1*$^{NTR\text{-}mCherry}$*; kdrl:EGFP* and *pdgfrb:GFP; kdrl:mCherry* embryos, respectively. Arterial and venous ISV identity was determined based on the connection to either the dorsal aorta (DA) or posterior caudal vein (PCV), respectively. Each data point represents the average cell number of 8–10 ISVs from an individual embryo. Data are plotted with mean ± SEM indicated. n = 11–15 (*nkx3.1*$^{NTR\text{-}mCherry}$*; kdrl:EGFP*) and 17 (*pdgfrb:GFP; kdrl: mCherry*) embryos at each time point. (B) *pdgfrb*$^{NTR\text{-}mCherry}$*; col1a2:GFP* embryos were imaged at 4 dpf to visualize perivascular fibroblasts and pericytes. No overlap in marker expression was observed between *pdgfrb*$^{NTR\text{-}mCherry}$-positive pericytes (red, arrows) and *col1a2:GFP*-positive perivascular fibroblasts (green, arrowheads). Unlike perivascular fibroblasts, pericytes also displayed elongated cellular processes (notched arrowheads). n = 14 embryos. (C) *pdgfrb*$^{NTR\text{-}mCherry}$*; kdrl:EGFP* embryos were imaged at 3 dpf to visualize individual pericytes (green, asterisks) with long cellular processes (notched arrowheads) that wrapped around the ISV (red). (D) Mosaic *col1a2*^{Kaede} line was imaged to visualize a single perivascular fibroblast (green, asterisks) associated with an ISV (red) in *col1a2*^{Kaede}*; kdrl:mCherry* embryos at 3 dpf. (E-I) Cell morphology, number of processes, and process length were quantified and graphed for single perivascular fibroblasts and pericytes using ImageJ as shown in (E). Perivascular fibroblasts showed an overall globular morphology as indicated by smaller aspect ratio (F) with more abundant (G) but shorter processes (H, I) compared to pericytes. n = 13 cells (perivascular fibroblasts), and 10 cells (pericytes). Data are plotted as mean ± SEM. Statistics: Mann-Whitney U test. Asterisk representation: p-value < 0.05 (*), p-value < 0.01 (**), p-value < 0.001 (***). Scale bars: (B) 25 μm; (C,D) 10 μm.

https://doi.org/10.1371/journal.pgen.1008800.g003

GFP did not express the *pdgfrb*$^{NTR\text{-}mCherry}$ reporter at 4 dpf. Conversely, *pdgfrb*$^{NTR\text{-}mCherry}$-positive pericytes at 4 dpf showed minimal *col1a2:GFP* expression. Further, while perivascular fibroblasts appeared globular, pericytes were more elongated with long cellular processes (Fig 3B). Perivascular fibroblasts were also more laterally located along ISVs compared to pericytes, with pericyte processes often sandwiched between the neighboring perivascular fibroblasts and the endothelium (Fig 3B). To further examine the morphological differences between perivascular fibroblasts and pericytes, we performed high resolution confocal microscopy at the single cell resolution at 3 dpf. *pdgfrb*$^{NTR\text{-}mCherry}$-positive pericytes showed the typical pericyte morphology: small and flat cell bodies with several elongated cellular processes that extended longitudinally along and tightly wrapped around the ISV, labeled by *kdrl:EGFP* (Fig 3C). Since perivascular fibroblasts are more abundant along ISVs compared to pericytes, we took advantage of a mosaic *col1a2:Gal4; UAS:Kaede* line (referred to as *col1a2*^{Kaede}) [50] to sparsely label single perivascular fibroblasts for easier visualization. Unlike the tight association between pericyte and the endothelium (10/10, Fig 3C), 36% of perivascular fibroblasts (5/14) showed visible gaps between the cell body and the underlying endothelium (Fig 3D), suggesting a looser association. In contrast to pericytes, perivascular fibroblasts had a globular morphology with short processes that wrapped diametrically around the associated ISV in an 'awkward hug' (Fig 3D). Quantification of cellular morphologies revealed key differences between these two cell types (Fig 3E–3I). In contrast to perivascular fibroblasts, pericytes displayed a significantly larger aspect ratio (Fig 3F), suggesting that they were more elongated along the long axis of the ISVs. Moreover, perivascular fibroblasts possessed more but shorter cellular processes compared to pericytes (Fig 3G–3I). Taken together, our results suggest that perivascular fibroblasts and pericytes represent two distinct populations of perivascular cells with unique marker expression, morphology, distribution and developmental timing.

A sub-population of perivascular fibroblasts functions as pericyte progenitors

While occupying the similar perivascular space, perivascular fibroblasts appear along ISVs at least one day before pericytes (Fig 3A). We hypothesized that perivascular fibroblasts act as progenitors for ISV pericytes. To test this possibility, we conducted time-lapse imaging of *pdgfrb*$^{NTR\text{-}mCherry}$*; col1a2:GFP* embryos from 54 to 73 hpf during which pericytes started to appear on ISVs. Interestingly, a subset of *col1a2:GFP*-positive perivascular fibroblasts gradually lost GFP expression, switched on the pericyte reporter *pdgfrb*$^{NTR\text{-}mCherry}$, and developed long cellular processes characteristic of pericytes at this stage (Fig 4A and S2 Video). Indeed, of 15

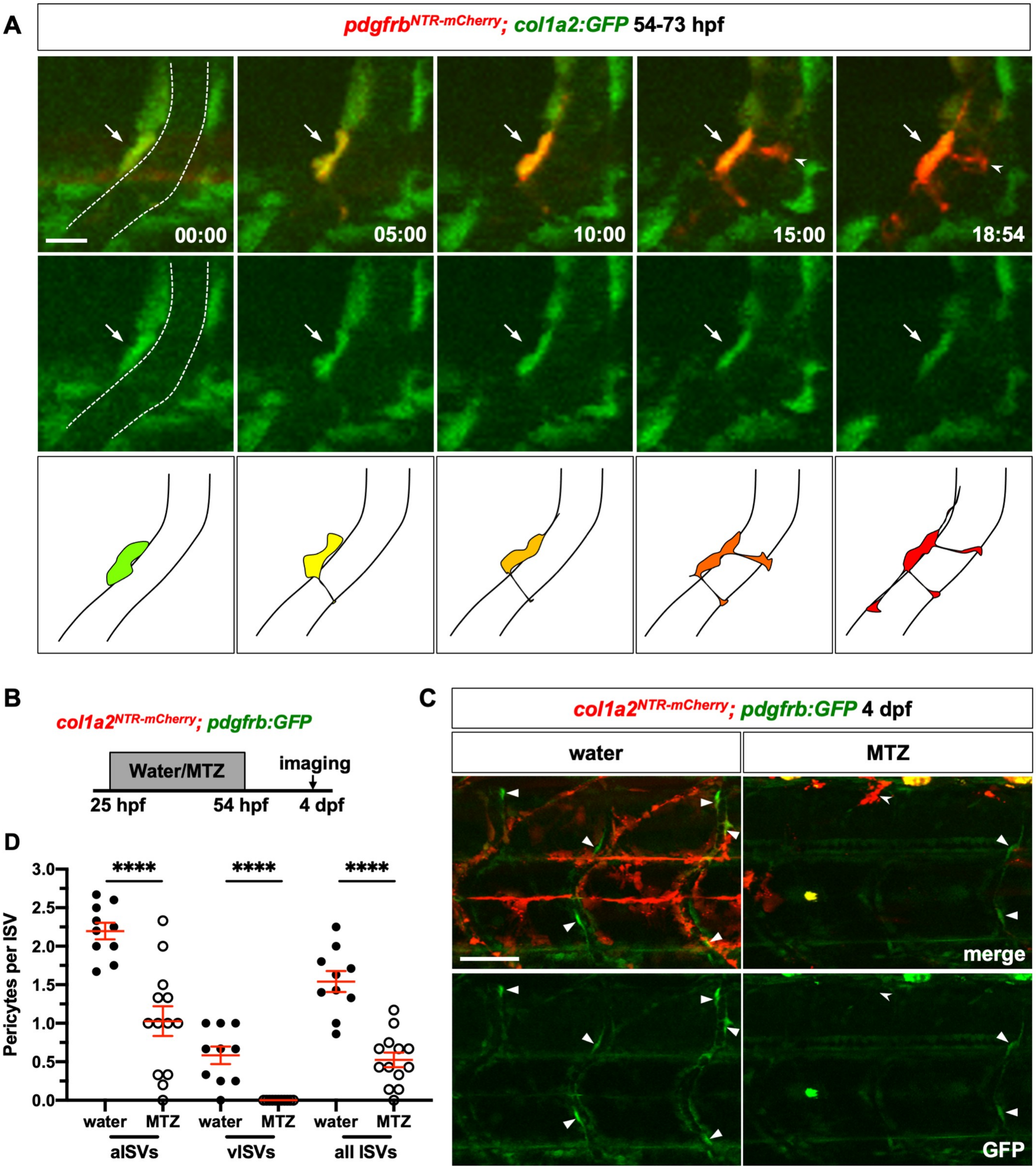

Fig 4. Perivascular fibroblasts function as pericyte progenitors. (A) Snapshots from time-lapse imaging of *pdgfrb*$^{NTR\text{-}mCherry}$; *col1a2:GFP* embryos from 54 to 73 hpf. Newly differentiated pericytes were retrospectively traced to identify their cell of origin. The ISV is outlined by dotted lines at the first time point. One perivascular fibroblast (green, arrows) traced can be seen gradually upregulating *pdgfrb*$^{NTR\text{-}mCherry}$ expression and extending pericyte-like cellular processes (notched arrowheads).

The time stamps are indicated in the hh:mm format. Schematic drawings of the merged images at each time point are shown at the bottom. The corresponding time-lapse movie is shown in S2 Video. $n = 7$ embryos. (B) Schematic showing experimental timeline of perivascular fibroblast ablation. *col1a2*$^{NTR\text{-}mCherry}$; *pdgfrb*:*GFP* embryos were incubated in either water or metronidazole (MTZ) from 25 to 54 hpf following which embryos were washed at 54 hpf and imaged at 4 dpf to visualize pericytes. (C) Representative images of water (left) or MTZ (right) treated *col1a2*$^{NTR\text{-}mCherry}$; *pdgfrb*:*GFP* embryos at 4 dpf. Compared to water-treated control embryos, MTZ-treated embryos showed complete ablation of mCherry$^+$ cells with only residual mCherry$^+$ debris (notched arrowheads). Fewer *pdgfrb*:*GFP*^{high} pericytes (arrowheads) can be seen in MTZ-treated embryos compared to water-treated controls. (D) Quantification of pericyte number after perivascular fibroblast ablation along aISVs and vISVs. Pericytes were identified based on high level expression of the *pdgfrb*:*GFP* reporter as shown in (C) and S3A and S3C Fig. Arterial versus venous ISVs were determined based on direction of the blood flow in each vessel. From each embryo, 8–10 ISVs in the mid-trunk region were imaged and scored. The average number of pericytes on aISVs, vISVs, or all ISVs were plotted in the graph with each data point representing one individual embryo. Pericytes were lost along both aISVs and vISVs after MTZ treatment. $n = 10$ (water) and 13 (MTZ) embryos. Data are plotted as mean ± SEM. Statistics: Mann-Whitney *U* test. Asterisk representation: p-value < 0.0001 (****). Scale bars: (A) 10 μm; (C) 50 μm.

https://doi.org/10.1371/journal.pgen.1008800.g004

newly formed pericytes traced in our time-lapse movies, 60% were derived from *col1a2*:*GFP*-expressing perivascular fibroblasts (9/15 cells). This result suggests that a sub-population of perivascular fibroblasts can differentiate into pericytes. Since *col1a2* transgenic lines such as *col1a2*:*GFP* are mosaic (S1A and S3E Fig) [50], the number above likely under-estimates the proportion of pericytes derived from perivascular fibroblasts. To further test our model, we performed time-lapse experiments in *nkx3.1*$^{NTR\text{-}mCherry}$; *pdgfrb*:*GFP* embryos. Similar to movies in *pdgfrb*$^{NTR\text{-}mCherry}$; *col1a2*:*GFP* embryos, cell tracing in *nkx3.1*$^{NTR\text{-}mCherry}$; *pdgfrb*:*GFP* embryos showed that about 8% of mCherry$^+$GFP^{low} perivascular fibroblasts (100/1208 cells) at 54 hpf slowly upregulated GFP expression, and extended pericyte-like cellular processes wrapping around the ISV (S3 Video). Of 125 newly formed GFP^{high} pericytes, 90% of them (113/125 cells) were derived from mCherry$^+$ cells, including perivascular fibroblasts residing along the ISV (101/113 cells), cells migrating from near the dorsal aorta (5/113 cells), as well as some cells with unclear origin due to incomplete imaging (7/113 cells). This result confirms that a sub-population of perivascular fibroblasts functions as pericyte precursors. Since perivascular fibroblasts originate from the sclerotome, we conclude that most pericytes along ISVs are also derived from the sclerotome.

To further test if perivascular fibroblasts serve as pericyte precursors, we performed genetic ablation of perivascular fibroblasts using the *col1a2*:*Gal4; UAS*:*NTR-mCherry* line (referred to as *col1a2*$^{NTR\text{-}mCherry}$). Nitroreductase (NTR) converts metronidazole (MTZ), an otherwise harmless prodrug into a cytotoxic compound, resulting in the death of NTR-expressing cells [51]. To ablate perivascular fibroblasts prior to pericyte differentiation, *col1a2*$^{NTR\text{-}mCherry}$; *pdgfrb*:*GFP* embryos were treated with MTZ from 25 to 54 hpf, after which the drug was washed off and embryos were imaged for pericytes at 4 dpf (Fig 4B). In contrast to water-treated controls, we observed a complete loss of perivascular fibroblasts in MTZ-treated embryos, with only residual mCherry$^+$ debris visible in the trunk (Fig 4C). Interestingly, we observed a substantial loss of pericytes on both arterial ISVs (aISVs) and venous ISVs (vISVs) in MTZ-treated embryos compared to water-treated controls (Fig 4D). This result is consistent with our model that perivascular fibroblasts function as pericyte precursors on both arteries and veins as depletion of perivascular fibroblasts leads to universal decrease in pericyte number on all ISVs. Together, our work suggests that the sclerotome generates perivascular fibroblasts, some of which further differentiate into pericytes along the ISVs.

Loss of perivascular fibroblasts results in dysmorphic ISVs

Our work suggests that perivascular fibroblasts function as progenitors to generate pericytes to support the vasculature. However, only a small fraction of perivascular fibroblasts actually differentiates into pericytes, raising question about the function of the remaining perivascular fibroblasts. Moreover, the emergence of perivascular fibroblasts occurs concurrently with ISV development (Figs 2B and S2A; S1 Video), well before pericyte differentiation at 60 hpf [43].

These observations raise the possibility that perivascular fibroblasts play an early role in stabilizing nascent blood vessels prior to pericyte formation. To test this idea, we examined the impact of early ablation of perivascular fibroblasts on ISV development using the nitroreductase-based system. *nkx3.1*$^{NTR\text{-}mCherry}$; *kdrl*:*EGFP* embryos were incubated in water or MTZ for a 24 hour period starting at 38 hpf when ISV formation was complete and blood flow had commenced in ISVs (Fig 5A). ISV morphology was examined after the drug treatment at 62 hpf. Water-treated control embryos showed stereotypical ISVs with many mCherry$^+$ perivascular fibroblasts (Fig 5B). MTZ treatment resulted in a complete loss of perivascular fibroblasts, with only some mCherry$^+$ cell debris remaining (Fig 5B). Compared to control ISVs, most ISVs in ablated embryos showed visible distortions in their diameters, shrinking and dilating dramatically at different points along their length (Fig 5B). To quantify this variability, the diameter of each ISV was measured at four equidistant points along its length and standard deviation from the mean diameter was graphed as a readout for ISV diameter variability (Fig 5C). Indeed, ISVs in the absence of perivascular fibroblasts were significantly more variable than those of water-treated controls (Fig 5C). Examination of larger blood vessels in the trunk revealed that MTZ treated embryos also showed significantly reduced mean diameter for both the dorsal aorta (DA) and posterior cardinal vein (PCV), with substantial increase in PCV diameter variability (S4 Fig). These results suggest that sclerotome derived cells play a crucial role in maintaining the trunk vasculature during the early stage. Interestingly, similar ablation experiments using *col1a2*$^{NTR\text{-}mCherry}$; *kdrl*:*EGFP* during later stages between 4 and 5 dpf did not significantly alter the ISV morphology (S5A–S5C Fig). Together, our results suggest that perivascular fibroblasts play an early role in the stabilization of nascent blood vessels but are dispensable for maintaining ISV morphology at later stages.

Perivascular fibroblasts deposit collagens around ISVs

Our work suggests that perivascular fibroblasts are crucial for the stabilization of nascent ISVs. Since perivascular fibroblasts show high-level expression of collagen genes, including *col1a2* and *col5a1*, we predicted that perivascular fibroblasts are the main source of the vascular ECM around newly formed ISVs. To test this model, we generated a *UAS*:*Col1a2-GFP* construct to express GFP-fused Col1a2 in live embryos. A similar *Col1a2-GFP* reporter has been previously used to visualize collagen deposition during skin development and repair in zebrafish [52]. *nkx3.1*:*Gal4; UAS*:*NTR-mCherry* embryos injected with the *UAS*:*Col1a2-GFP* plasmid showed many mCherry$^+$GFP$^+$ perivascular fibroblasts surrounding ISVs at 56 hpf (Fig 5D). Indeed, numerous thin GFP$^+$ 'strings', likely corresponding to collagen fibers, wrapped around the ISV with the intensity increasing from 56 to 72 hpf, suggesting continuous Col1a2-GFP protein deposition (Fig 5D). To determine whether perivascular fibroblasts directly contribute to collagens around ISVs, we injected *nkx3.1*$^{NTR\text{-}mCherry}$ embryos with a low dose of the *UAS*:*Col1a2-GFP* plasmid to achieve mosaic labeling of perivascular fibroblasts. Imaging of individually labeled mCherry$^+$GFP$^+$ perivascular fibroblasts showed local Col1a2-GFP deposition around the ISV within 1–2 cell diameters from the Col1a2-GFP-expressing perivascular fibroblast (Fig 5E). Our results suggest that perivascular fibroblasts contribute to collagens in the ECM surrounding nascent ISVs that likely contribute to vessel stabilization.

To visualize the dynamics of collagen deposition, we combined cell ablation experiments with a stable *UAS*:*Col1a2-GFP* transgenic line. *nkx3.1*:*Gal4; UAS*:*NTR-mCherry; UAS*:*Col1a2-GFP* (*nkx3.1*$^{NTR\text{-}mCherry;Col1a2\text{-}GFP}$) embryos were incubated in water or MTZ from 38 to 62 hpf (Fig 5F). Embryos were imaged individually before and after the water/MTZ treatment to compare collagen deposition around the same ISVs (Fig 5G). Water-treated control embryos showed an average of 27% increase in Col1a2-GFP protein deposition around ISVs

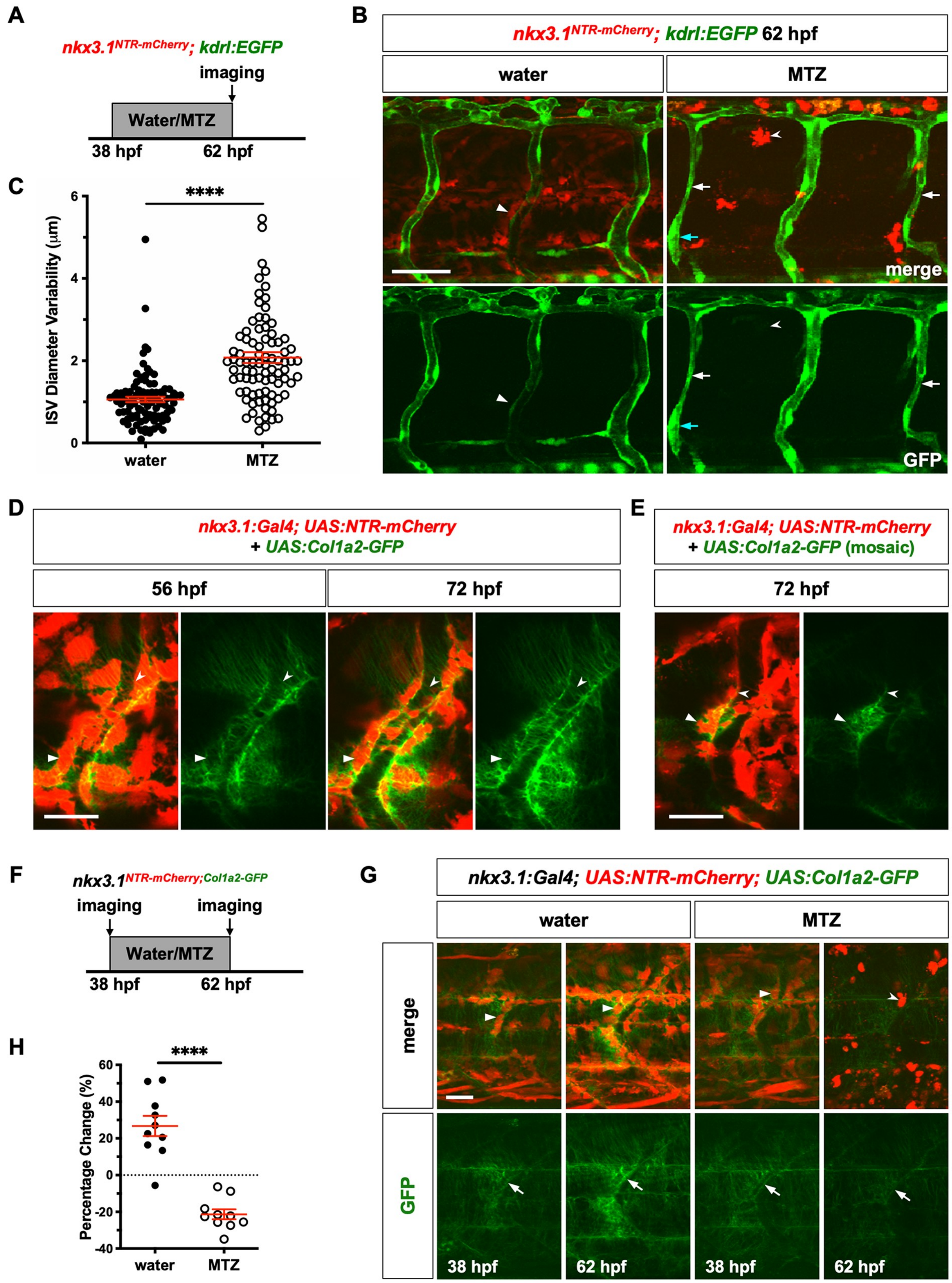
A
nkx3.1NTR-mCherry; kdrl:EGFP
imaging
Water/MTZ
38 hpf
62 hpf
B
nkx3.1NTR-mCherry; kdrl:EGFP 62 hpf
water
MTZ
merge
GFP
C
ISV Diameter Variability (μm)
****
water
MTZ
D
nkx3.1:Gal4; UAS:NTR-mCherry
+ UAS:Col1a2-GFP
56 hpf
72 hpf
E
nkx3.1:Gal4; UAS:NTR-mCherry
+ UAS:Col1a2-GFP (mosaic)
72 hpf
F
nkx3.1NTR-mCherry;Col1a2-GFP
imaging
imaging
Water/MTZ
38 hpf
62 hpf
G
nkx3.1:Gal4; UAS:NTR-mCherry; UAS:Col1a2-GFP
water
MTZ
merge
GFP
38 hpf
62 hpf
38 hpf
62 hpf
H
Percentage Change (%)
****
water
MTZ

Fig 5. Perivascular fibroblasts stabilize nascent blood vessels by collagen deposition. (A) Schematic of experimental protocol for early ablation of perivascular fibroblasts. *nkx3.1*$^{NTR\text{-}mCherry}$*; kdrl:EGFP* embryos were incubated in either water or metronidazole (MTZ) from 38 to 62 hpf and imaged to visualize ISV morphology. (B) Representative images showing water (left) and MTZ (right) treated embryos. Water-treated control embryos had many mCherry$^+$ cells (arrowheads), while MTZ treatment resulted in complete ablation of mCherry$^+$ cells with only mCherry$^+$ debris (notched arrowheads) remaining. MTZ-treated embryos showed visibly deformed ISV morphology with greater variation in vessel diameter (the constricted and dilated regions of ISVs are indicated by white and cyan arrows, respectively) compared to uniform ISVs in controls. (C) Quantification of ISV diameter variability in (B). ISV diameter was measured at 4 equidistant points along each ISV using the line tool in ImageJ. Mean diameter of each ISV was calculated and standard deviation from the mean was plotted as a readout of diameter variability in each ISV examined. MTZ-treated embryos showed significantly more variable ISVs compared to water-treated controls. Vessel diameter and variability measurements for the dorsal aorta and posterior cardinal vein are shown in S4 Fig. *n* = 98 ISVs from 11 embryos (water); 86 ISVs from 10 embryos (MTZ). Results are graphed as mean ± SEM. Statistics: Mann-Whitney *U* test. Asterisk representation: p-value < 0.0001 (****). (D) *nkx3.1*$^{NTR\text{-}mCherry}$ embryo were injected with the *UAS:Col1a2-GFP* plasmid and imaged at 56 and 72 hpf. Many mCherry$^+$GFP$^+$ perivascular fibroblasts (arrowheads) can be seen surrounding the ISV. Numerous thin GFP$^+$ collagen fibers (notched arrowheads) wrapped around the ISV and the Col1a2-GFP protein deposition appeared to increase from 56 to 72 hpf. *n* = 16 embryos. (E) *nkx3.1*$^{NTR\text{-}mCherry}$ embryos were injected with a low dose of the *UAS: Col1a2-GFP* plasmid and imaged at 72 hpf. Col1a2-GFP deposition (notched arrowheads) around an ISV by a single mCherry$^+$GFP$^+$ perivascular fibroblast (arrowheads) can be seen. *n* = 16 embryos. (F) Schematic of experimental protocol to examine collagen deposition after early ablation of perivascular fibroblasts. *nkx3.1:Gal4; UAS:NTR-mCherry; UAS:Col1a2-GFP* embryos were incubated in water or metronidazole (MTZ) from 38 to 62 hpf. The same mid-trunk region of individual embryos was imaged prior to and after the drug treatment to visualize Col1a2-GFP deposition. (G) Representative images of water (left) and MTZ (right) treated embryos before and after the drug treatment. Water-treated control embryos showed many mCherry$^+$ cells (arrowheads), while MTZ treatment resulted in complete ablation of mCherry$^+$ cells with only mCherry$^+$ debris (notched arrowhead) remaining post treatment. Control embryos showed an obvious increase in Col1a2-GFP deposition around ISVs (arrows) from 38 to 62 hpf, while MTZ treated embryos showed reduction in Col1a2-GFP during the same time period. (H) Quantification of changes in fluorescence intensity of Col1a2-GFP in (G). GFP intensity was measured for each embryo before and after the drug treatment and percentage change in GFP intensity was calculated using the following formula: $(GFP_{after}—GFP_{before}) / GFP_{before} \times 100\%$. *n* = 10 embryos in each condition. Data are plotted as mean ± SEM. Statistics: Mann-Whitney *U* test. Asterisk representation: p-value < 0.0001 (****). Scale bars: (B) 50 μm; (D,E,G) 25 μm.

https://doi.org/10.1371/journal.pgen.1008800.g005

(Fig 5G and 5H). By contrast, complete ablation of perivascular fibroblasts with MTZ treatment resulted in a 21% decrease in Col1a2-GFP signal (Fig 5G and 5H). This result suggests that perivascular fibroblasts play an active role in contributing to collagens in the vascular ECM during early stages of ISV development. To determine whether perivascular fibroblasts continue to deposit collagens at later stages, we performed similar cell ablation experiments in *col1a2*$^{NTR\text{-}mCherry;Col1a2\text{-}GFP}$ embryos from 4 to 5 dpf (S5D Fig). Water-treated controls showed 8% increase in Col1a2-GFP level around ISVs, whereas collagen deposition in MTZ-treated embryos remained largely unchanged (S5E and S5F Fig). In summary, these results show that the vascular collagen network undergoes active remodeling during initial development, but becomes more stable at later stages, highlighting the early requirement of perivascular fibroblasts.

collagen mutants show severe ISV hemorrhage

Our work suggests that perivascular fibroblasts secrete collagens and stabilize nascent ISVs. We next asked whether Col1a2 and Col5a1, which are expressed in perivascular fibroblasts (Figs 1C and S1B), are required to maintain the integrity of nascent blood vessels. Using CRISPR/Cas9 editing [53], we generated mutants for *col1a2* (*col1a2*^{ca108}, 1-bp deletion) and *col5a1* (*col5a1*^{ca109}, 4-bp deletion) (S6A and S6B Fig). Both alleles resulted in frame shifts in the corresponding coding sequences leading to premature stops (S6C and S6D Fig). For simplicity, we designate wild-type, heterozygous or homozygous fish as +/+, +/-, and -/-, respectively. For example, heterozygous carriers of *col1a2*^{ca108} are referred to as *col1a2*$^{+/-}$. Whole mount in situ hybridization showed that mutant mRNAs for both genes underwent nonsense-mediated decay (Fig 6A), suggesting that both *col1a2*^{ca108} and *col5a1*^{ca109} are null alleles. Crosses of heterozygous *col1a2*$^{+/-}$ parents gave rise to progeny segregated in roughly Mendelian ratios at all stages examined (S7A Fig). Although homozygous *col1a2*$^{-/-}$ mutants were viable as adults, they were substantially smaller than their wild-type siblings and often showed severe spine curvature (S7B Fig). This phenotype is reminiscent of those described in other type I collagen mutants [54, 55]. By contrast, from crosses of heterozygous *col5a1*$^{+/-}$ parents,

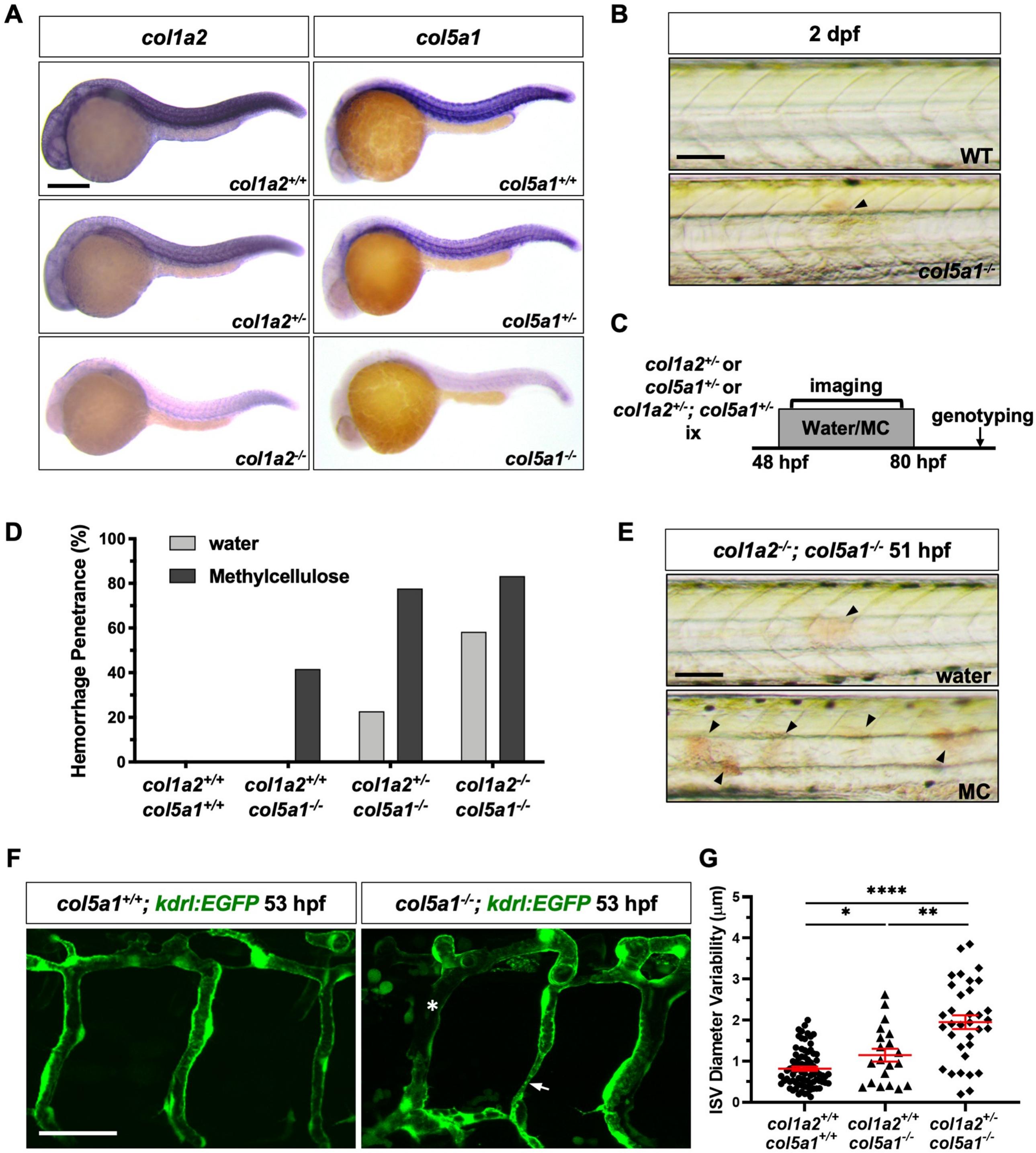

Fig 6. Characterization of collagen mutants. (A) Embryos from intercrosses of *col1a2*$^{+/-}$ adults or *col5a1*$^{+/-}$ adults were stained at 24 hpf by mRNA in situ hybridization with *col1a2* (left) or *col5a1* (right) probes, respectively. Compared to wild type siblings, heterozygous mutants showed reduced staining, and homozygous mutants displayed an almost complete loss of staining for both genes examined. n = 30 embryos for each staining. (B) *col5a1*$^{-/-}$ mutants but not wild-type siblings showed spontaneous hemorrhage in the trunk (arrowhead) at 2 dpf. (C) Schematic of experimental protocol for phenotypic analysis of collagen mutants. Embryos from intercrosses of 1) *col1a2*$^{+/-}$ adults, 2) *col5a1*$^{+/-}$ adults, or 3) *col1a2*$^{+/-}$; *col5a1*$^{+/-}$ adults were incubated in either water or 0.6% methylcellulose (MC) and screened for the hemorrhage phenotype in the trunk from 48 to 80 hpf. All embryos were subsequently genotyped. (D)

Quantification of hemorrhage penetrance of embryos from intercrosses of *col1a2*$^{+/-}$; *col5a1*$^{+/-}$ adults described in (C). The hemorrhage penetrance was calculated by dividing the number of embryos with the hemorrhage phenotype by the total number of embryos of the same genotype. n = 12 (*col1a2*$^{+/+}$; *col5a1*$^{+/+}$ + water); 9 (*col1a2*$^{+/+}$; *col5a1*$^{+/+}$ + MC); 12 (*col1a2*$^{+/+}$; *col5a1*$^{-/-}$ + water); 12 (*col1a2*$^{+/+}$; *col5a1*$^{-/-}$ + MC); 22 (*col1a2*$^{+/-}$; *col5a1*$^{-/-}$ + water); 27 (*col1a2*$^{+/-}$; *col5a1*$^{-/-}$ + MC); 12 (*col1a2*$^{-/-}$; *col5a1*$^{-/-}$ + water); and 18 (*col1a2*$^{-/-}$; *col5a1*$^{-/-}$ + MC) embryos. (E) In experiments described in (C), embryos were imaged 3 hours after incubation in water (top) or MC (bottom) at 2 dpf and subsequently genotyped. MC-treated *col1a2*$^{-/-}$; *col5a1*$^{-/-}$ embryos showed an increase in the number of hemorrhage foci (arrowheads) compared to water-treated controls. Quantification of this result is shown in S7D Fig. (F) Embryos from crosses of *col1a2*$^{+/-}$; *col5a1*$^{+/-}$ and *col5a1*$^{+/-}$; *kdrl:EGFP* adults were incubated in the 0.6% methylcellulose solution at 48 hpf, and their ISVs were imaged at 53 hpf. *col5a1*$^{-/-}$; *kdrl:EGFP* embryos showed visible ISV constrictions (arrow) and broken ISVs (asterisk) compared to *col5a1*$^{+/+}$; *kdrl:EGFP* siblings. (G) Quantification of ISV diameter variability in embryos from crosses of *col1a2*$^{+/-}$; *col5a1*$^{+/-}$ and *col5a1*$^{+/-}$; *kdrl:EGFP* adults as described in (F). ISV diameter and variability were measured as described in Fig 5. n = 81 ISVs from 10 embryos (*col1a2*$^{+/+}$; *col5a1*$^{+/+}$; *kdrl:EGFP*); 20 ISVs from 3 embryos (*col1a2*$^{+/+}$; *col5a1*$^{-/-}$; *kdrl:EGFP*); and 34 ISVs from 4 embryos (*col1a2*$^{+/-}$; *col5a1*$^{-/-}$; *kdrl:EGFP*). Data are graphed as mean ± SEM. Statistics: Mann-Whitney U test. Asterisk representation: p-value < 0.05 (*); p-value < 0.01 (**); p-value < 0.0001 (****). Scale bars: (A) 250 μm; (B,E) 100 μm; (F) 50 μm.

https://doi.org/10.1371/journal.pgen.1008800.g006

homozygous *col5a1*$^{-/-}$ mutants were under-represented at 11 dpf, and completely absent by 14 dpf (S7C Fig). These results suggest that Col5a1 is a more critical component of the ECM compared to Col1a2, and it is required for the survival of the fish to adulthood. Strikingly, a small percentage of embryos from crosses of heterozygous *col5a1*$^{+/-}$ parents (2/88: 2%) showed spontaneous hemorrhage in the trunk region at 2 dpf and were genotyped as homozygous *col5a1*$^{-/-}$ (Fig 6B), suggesting compromised vascular integrity in the absence of Col5a1.

To further characterize the hemorrhage phenotype in *collagen* mutants, we developed a phenotype screening procedure (Fig 6C). In this assay, we analyzed both single mutants as well as double mutants to test genetic interactions between *col1a2* and *col5a1*. In addition, we tested whether the increase in physical stress exacerbates the hemorrhage phenotype by raising embryos in a high-viscosity medium (0.6% methylcellulose, MC) [56]. Briefly, heterozygous adults harboring either one or both of the *collagen* mutations (*col1a2*$^{+/-}$, *col5a1*$^{+/-}$, or *col1a2*$^{+/-}$; *col5a1*$^{+/-}$) were intercrossed to generate wild type, heterozygous, and homozygous sibling embryos for different combinations (Fig 6C). The resulting embryos were then incubated in either water or the viscous methylcellulose solution from 48 to 80 hpf, during which embryos were imaged and screened for hemorrhage in the trunk. Embryos were then genotyped to correlate the genotype with the phenotype. Similar to their wild-type *col1a2*$^{+/+}$ siblings (water: 0/14; MC: 0/27) and heterozygous *col1a2*$^{+/-}$ siblings (water: 0/39; MC: 0/38), homozygous *col1a2*$^{-/-}$ mutants did not show any trunk hemorrhage in either water (0/22) or the methylcellulose solution (0/21). This result suggests that loss of *col1a2* alone does not compromise vascular stability even with increased physical stress. By contrast, while neither wild-type *col5a1*$^{+/+}$ embryos (0/11) nor heterozygous *col5a1*$^{+/-}$ siblings (0/39) showed any hemorrhage under normal conditions, 12% of *col5a1*$^{-/-}$ embryos (3/25) displayed obvious hemorrhages in the trunk at 2 dpf, which was worsened substantially by physical stress (17/26, 65%). Analysis of different allele combinations of double mutants revealed several key characteristics of the hemorrhage phenotype (Fig 6D). First, the loss of both *col5a1* wild-type alleles was required to cause the trunk hemorrhage phenotype. Second, even though loss of *col1a2* alone in *col1a2*$^{+/-}$ or *col1a2*$^{-/-}$ embryos was not sufficient to cause hemorrhage, loss of one or two *col1a2* wild-type alleles progressively increased the penetrance of the hemorrhage phenotype in *col5a1*$^{-/-}$ mutants, from 23% in *col1a2*$^{+/-}$; *col5a1*$^{-/-}$ embryos (5/22) to 58% in *col1a2*$^{-/-}$; *col5a1*$^{-/-}$ embryos (7/12) (Fig 6D). Lastly, increased physical stress by incubating embryos in the viscous methylcellulose solution substantially exacerbated both the penetrance and the severity of the hemorrhage phenotype (Figs 6D, 6E and S7D). It is interesting to note that stress-induced blood vessel rupture is typical of the vascular phenotypes associated with classical Ehlers-Danlos syndrome in humans. Together, our mutant analysis suggests that Col5a1 and Col1a2 function redundantly to maintain blood vessel integrity with Col5a1 being a more critical component.

The distribution of hemorrhagic foci is consistent with defects in ISVs in the trunk. To directly examine the ISV morphology in *collagen* mutants, we crossed *col5a1*$^{+/-}$; *kdrl:EGFP* adults with *col1a2*$^{+/-}$; *col5a1*$^{+/-}$ double heterozygous fish. Resulting embryos were incubated in the methylcellulose solution and their ISVs were analyzed at 53 hpf. In contrast to wild-type siblings, some *col5a1*$^{-/-}$ mutants showed severe ISV deformity and breakage, accompanied by hemorrhage (Fig 6F). It is likely that the hemorrhage phenotype is caused by physical forces exerted on fragile and deformed ISVs during muscle contractions. Quantifications of the diameter variability of intact ISVs as described earlier showed that both *col1a2*$^{+/+}$; *col5a1*$^{-/-}$ and *col1a2*$^{+/-}$; *col5a1*$^{-/-}$ embryos displayed significantly more variable ISVs than wild-type siblings (Fig 6G). Consistent with a stronger hemorrhage phenotype, ISVs in *col1a2*$^{+/-}$; *col5a1*$^{-/-}$ embryos were significantly more variable than those in *col1a2*$^{+/+}$; *col5a1*$^{-/-}$ single mutants. Together, our work suggests that the deposition of Col5a1 and Col1a2 between 1–2 dpf, likely by perivascular fibroblasts, is crucial for the stabilization of nascent ISVs.

Discussion

In this study, we characterize the origin and function of perivascular fibroblasts, a novel population of blood vessel associated cells in zebrafish. Our work provides three main conclusions. First, perivascular fibroblasts originate from the sclerotome and are distinct from pericytes. Second, a subset of perivascular fibroblasts functions as pericyte progenitors. Third, cell ablation and mutant analysis reveal that perivascular fibroblasts stabilize nascent blood vessels through deposition of collagens, including Col1a2 and Col5a1. Together, we propose a dual role of perivascular fibroblasts in vascular stabilization: they first establish the ECM around nascent blood vessels for initial stabilization and then function as pericyte progenitors to generate pericytes that further contribute to vessel integrity (Fig 7). Our work provides new insights into the molecular and cellular mechanisms underlying vascular stabilization and vascular diseases, such as Ehlers-Danlos syndrome.

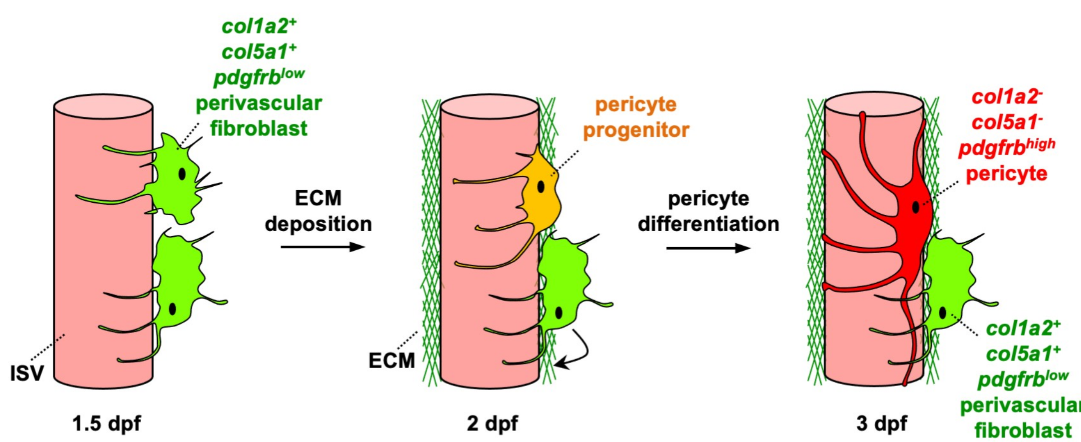

Fig 7. Model of perivascular fibroblasts in vascular stabilization in zebrafish. Perivascular fibroblasts, characterized by the expression of fibrillar collagens *col1a2* and *col5a1* as well as low levels of *pdgfrb*, become associated with intersegmental vessels (ISVs) in the zebrafish trunk by 1.5 dpf. Perivascular fibroblasts deposit a network of collagen fibers to establish the vascular ECM and stabilize nascent ISVs at 2 dpf and continue to deposit collagen until at least 3 dpf. In the same time window, a subset of perivascular fibroblasts functions as pericyte progenitors. They gradually upregulate the expression of the classic pericyte marker *pdgfrb* and develop elongated cellular processes. By 3 dpf, these 'pericyte progenitors' have completely differentiated into mature pericytes, showing robust *pdgfrb* expression distinct from collagen-expressing perivascular fibroblasts. Together, perivascular fibroblasts perform dual functions in vascular stabilization by depositing collagens to support nascent blood vessels and acting as pericyte progenitors.

https://doi.org/10.1371/journal.pgen.1008800.g007

Perivascular fibroblasts are a unique population of perivascular cells

Pericytes are well studied blood vessel support cells associated with intersegmental vessels in the zebrafish trunk. Four lines of evidence suggest that collagen-expressing perivascular fibroblasts represent a unique population of perivascular cells, distinct from mature and fully differentiated pericytes. First, these two cell populations show distinct marker expression, with fully differentiated pericytes labeled by high level of *pdgfrb* expression, whereas perivascular fibroblasts marked by the expression of collagen genes, such as *col1a2* and *col5a1*. Second, perivascular fibroblasts become associated with ISVs as early as 31 hpf, whereas pericytes do not differentiate until at least 60 hpf [43]. Third, perivascular fibroblasts are much more abundant than pericytes, and are associated with both arterial and venous ISVs in similar numbers unlike pericytes. Finally, perivascular fibroblasts are positioned abluminal to pericytes and appear more globular with numerous shorter processes that extend around the endothelium. Based on the differences in marker expression, developmental timing, cell number, and cell morphology, we propose that perivascular fibroblasts represent a novel perivascular cell population, distinct from pericytes. Intriguingly, several single cell RNA sequencing studies have revealed a similar perivascular 'fibroblast-like' cell population in the adult murine brain [28–31]. Murine fibroblast-like cells show robust expression of ECM genes, including collagen genes *col5a1* and *col1a2*, but much less mural cell markers such as *pdgfrb* [31, 57]. Furthermore, similar to zebrafish, murine perivascular fibroblast-like cells are loosely adhered to the blood vessels, abluminal to mural cells and the basement membrane [31]. Combined with our work, these studies suggest that perivascular fibroblasts represent a unique and evolutionarily conserved population of blood vessel associated cells across vertebrates.

The sclerotome is the embryonic origin of perivascular fibroblasts and pericytes

The sclerotome is the embryonic compartment that contributes to the axial skeleton of vertebrates. Our previous and current studies demonstrate that the sclerotome also gives rise to several populations of tissue support cells, including tenocytes (tendon fibroblasts) [44] and perivascular fibroblasts. The zebrafish sclerotome has a unique bipartite organization with a larger ventral domain and a smaller dorsal domain. Using time-lapse imaging and cell tracing, we have built a spatial map of origin for perivascular fibroblasts. Similar to tenocytes, different sclerotome domains contribute to perivascular fibroblasts in a stereotypic spatial pattern, with the ventral sclerotome domain being the major contributor (84%). The ventral sclerotome domain generates perivascular fibroblasts along the entire length of the ISV, whereas the dorsal sclerotome domain contributes only locally to perivascular fibroblasts associated with the dorsal half of the ISV.

Since perivascular fibroblasts also function as pericyte precursors (see below), our results suggest that most pericytes associated with ISVs also originate from the sclerotome. Consistent with our results, vSMCs around the dorsal aorta have been traced back to cells derived from the sclerotome in zebrafish [49]. In addition, mural cells in the zebrafish trunk vessels have been shown to be dependent on the mesoderm but not the neural crest lineage [58]. Thus, blood vessel support cells in the zebrafish trunk, including perivascular fibroblasts and mural cells, likely originate from the sclerotome. Combined with previous lineage analysis in mouse and chick [59, 60], these data suggest a model where mural cells in the brain are neural crest derived, whereas mural cells in the trunk are sclerotome derived.

Perivascular fibroblasts function as pericyte progenitors

Although perivascular fibroblast-like cells have been identified in the mouse brain by single cell RNA sequencing, their biological functions are still unclear. In our study, in vivo time-lapse imaging reveals that the majority of newly born pericytes on ISVs at 3 dpf can be traced back to perivascular fibroblasts at 2 dpf. In a complementary approach, we show that genetic ablation of perivascular fibroblasts results in a general reduction in the number of pericytes on both arterial and venous ISVs. Together, these results indicate that some perivascular fibroblasts serve as pericyte precursors, contributing to most, if not all, pericytes associated with ISVs in the trunk. Incomplete labeling or ablation likely reflects the mosaic nature of the *col1a2* transgenic lines [50].

It is interesting to note that there are about 10 perivascular fibroblasts associated with each ISV, however, only about 8% of these cells differentiate into pericytes. It thus raises the question of how these perivascular fibroblasts are 'selected' as pericyte progenitors. There are two possibilities. In the first scenario, all perivascular fibroblasts have the equal potential to differentiate into pericytes, but extrinsic cues determine which cell to switch on the pericyte fate. Notch signaling has been implicated in the regulation of pericyte formation in both mouse and zebrafish [58, 61–64]. In particular, recent work in zebrafish has shown that the activation of Notch signaling in naïve mesenchymal cells (likely corresponding to perivascular fibroblasts in our study) is crucial to induce pericyte differentiation around ISVs [58]. Therefore, active Notch signaling might bias some perivascular fibroblasts towards the pericyte lineage. Alternatively, perivascular fibroblasts might represent a heterogenous population of cells, containing a small fraction of pericyte progenitors. Supporting this idea, recent scRNA sequencing studies have shown that perivascular fibroblast-like cells in the mouse brain can be further divided into several subtypes based on unique gene expression signatures [30, 31].

Perivascular fibroblasts function to stabilize nascent blood vessels

Although mural cells are known to stabilize mature blood vessels, it is not clear how newly formed blood vessels are supported prior to the differentiation of mural cells. Our work provides strong evidence that perivascular fibroblasts function to stabilize nascent blood vessels by depositing collagens in the vascular ECM. Time-lapse imaging shows that the emergence of collagen-expressing perivascular fibroblasts along ISVs occurs concurrently with ISV development, at least one day before the differentiation of the first pericytes. The live Col1a2-GFP reporter reveals that perivascular fibroblasts contribute to a network of collagen fibers around nascent ISVs as early as 38 hpf, which continues to expand until at least 3 dpf. Consistent with this observation, genetic ablation of perivascular fibroblasts from 38 to 62 hpf prior to pericyte differentiation largely prevents the expansion of the collagen network around ISVs, leading to aberrant ISV morphology. These findings suggest that perivascular fibroblasts contribute to the collagen network to stabilize newly formed blood vessels before pericyte differentiation. Consistent with this model, loss of *col5a1* results in dysmorphic ISVs with spontaneous hemorrhage in the trunk, which is exacerbated by the additional loss of *col1a2* or increasing physical stress. Crucially, we find that these ISV phenotypes can be observed as early as 2 dpf, well before the emergence of first pericytes on ISVs. Consistent with our work, recent study has described a similar population of *col22a1*$^{+}$ perivascular fibroblast-like cells associated with the cranial vasculature in zebrafish [65]. Null mutations in *col22a1*, a minor fibril-associated collagen, result in compromised cranial vessel integrity in both embryos and adults following cardiovascular stress [65], highlighting the importance of collagen and perivascular fibroblasts in vascular stabilization.

Intriguingly, early ablation of perivascular fibroblasts rarely results in the severe hemorrhage phenotype observed in *col5a1*$^{-/-}$ mutants (under either normal or stressed conditions). Using the live Col1a2-GFP reporter, we find that low level of Col1a2-GFP deposition is already visible around ISVs at 38 hpf prior to MTZ treatment, some of which persists even after ablation at 62 hpf (Fig 5G). It is therefore possible that these residual collagen fibers provide sufficient support to newly formed ISVs and prevent severe hemorrhage seen in collagen mutants. It is also interesting to note that Col1a2-GFP level decreases substantially upon early but not late ablation of perivascular fibroblasts, indicating a higher turnover rate of collagen fibers during early stages of vascular development. This is supported by our observation that late ablation of perivascular fibroblasts from 4 to 5 dpf minimally impacts ISV morphology. Although our work points to perivascular fibroblasts as the main contributor of the vascular ECM, it remains possible that other cell type(s) in the vicinity, such as tenocytes, might contribute to collagen deposition around the ISVs. Development of specific genetic driver lines will allow us to directly test this possibility in the future.

Zebrafish model of Ehlers-Danlos syndrome

Collagen is the most abundant protein in the human body and is a major component of the ECM [66]. Fibrillar collagens, including collagen I and collagen V, constitute the most common subgroup within the collagen family which often co-localize in tissues such as the dermis, tendons and ligaments [66]. Mutations in fibrillar collagens or collagen modification enzymes have been implicated in a number of connective tissue diseases, including Ehlers-Danlos syndrome (EDS). The classical subtype of EDS, caused by mutations in collagen V, and less frequently collagen I, is characterized by skin hyperextensibility, joint hypermobility, and blood vessel fragility [19, 67]. Classical EDS patients experience easy bruising and excessive hemorrhaging under normal exertion. By contrast, vascular phenotypes are more prominent in the vascular subtype of EDS, resulting from mutations in collagen III, with most patients experiencing severe spontaneous rupture of large arteries [19]. Interestingly, the zebrafish genome does not contain a collagen III gene, which is likely lost during evolution as in many other teleost fish species [68]. Characterization of zebrafish *col1a2* and *col5a1* mutants reveals several key features of vascular EDS. Embryos lacking functional *col5a1* genes develop spontaneous hemorrhages in the trunk under normal physiological conditions, reminiscent of easy bruising in patients with vascular EDS. One hallmark of vascular EDS is that physical stress often leads to more severe symptoms [69]. Similarly, both the penetrance and severity of the hemorrhage phenotype in *col5a1*$^{-/-}$ mutants are strongly enhanced by the increase of physical stress. Thus, our results suggest that the lack of collagen III in zebrafish is likely compensated by other fibrillar collagens (types I and V). Our *col1a2* and *col5a1* mutants represent the first zebrafish model of vascular EDS that we know of.

Analysis of collagen mutants also provides new insights on vascular EDS. First, Col5a1 is a more critical component of the vascular ECM compared to Col1a2. Lack of *col5a1* function leads to ISV hemorrhages, whereas loss of *col1a2* alone does not result in any obvious vascular defects even with increased physical stress. Intriguingly, collagen I is the most abundant component in collagen fibrils ($> 90\%$), while collagen V constitutes only a minor fraction ($< 5\%$) [70]. Why do *col5a1*$^{-/-}$ mutants show more severe phenotypes than *col1a2*$^{-/-}$ mutants? Previous work has shown that Col5a1 plays an important role in proper nucleation and diameter regulation of collagen fibrils [71]. The loss of Col5a1 might result in defects in the assembly of collagen I into fibrils, leading to a more severe phenotype. Second, our mutant analysis reveals genetic interactions between *col1a2* and *col5a1*. Loss of wild-type *col1a2* alleles in the *col5a1*$^{-/-}$ background substantially enhances both the penetrance and the severity of the hemorrhage phenotype in a dosage dependent manner. This result suggests that Col5a1 and Col1a2 function redundantly to maintain vascular integrity. Lastly, as discussed above, our work provides strong evidence that defects in perivascular fibroblasts are the underlying cellular basis for the vascular phenotypes of EDS patients. Perivascular fibroblasts thus represent the cellular targets for potential therapeutic interventions.

In summary, our work identifies perivascular fibroblasts as a novel perivascular cell population with dual function in vascular stabilization: they regulate the ECM of nascent blood vessels and also function as pericyte progenitors. Interestingly, many perivascular fibroblasts remain associated with mature blood vessels even after pericyte differentiation. This raises several questions about the function of these cells at later stages. Do perivascular fibroblasts continue to regulate the ECM around the mature vasculature? Do they function as resident stem cells to replace aging/damaged pericytes? Previous work has suggested that tissue injury in the mouse brain and spinal cord often triggers a fibrotic response by blood vessel associated cells [25, 32–34]. Attenuation of the fibrotic response has been shown to limit scar formation and improve axon regeneration post spinal cord injury in mice, suggesting that perivascular stromal cells might be an important therapeutic target [72]. It is plausible that zebrafish perivascular fibroblasts also play an active role in tissue injury repair, an exciting question for future investigations.

Materials and methods

Zebrafish strains

Zebrafish strains were maintained according to standard protocols. Animal research was conducted in accordance with current guidelines of the Canadian Council on Animal Care. All protocols were approved by the Animal Care Committee at the University of Calgary (#AC17-0128). The following transgenic strains were utilized in this study: *TgBAC(col1a2:Gal4)ca102* [44, 50], *TgBAC(col1a2:GFP)ca103* [44], *Tg(kdrl:EGFP)la116* [73], *Tg(kdrl:mCherry)ci5* [74], *TgBAC(nkx3.1:Gal4)ca101* [44], *TgBAC(pdgfrb:Gal4FF)ca42* [48], *TgBAC(pdgfrb:GFP)ca41* [47], *Tg(UAS:Col1a2-GFP)ca111*, *Tg(UAS:Kaede)s1999t* [75], and *Tg(UAS:NTR-mCherry)c264* [75]. The mosaic *col1a2:Gal4; UAS:Kaede* line was maintained by growing embryos with more mosaic Kaede expression. The $col1a2^{ca108}$ and $col5a1^{ca109}$ mutant lines were maintained as heterozygotes, and homozygous embryos were generated by intercrossing heterozygous carriers.

Generation of CRISPR mutants

The $col1a2^{ca108}$ and $col5a1^{ca109}$ mutant lines were generated using the CRISPR/Cas9 system as previously described [53]. Briefly, target sites were identified using the web program CHOP-CHOP (http://chopchop.cbu.uib.no) [76]. sgRNA target sequences are 5'-GGGGGTTCCATTTGATCCAG-3' (*col1a2*) and 5'-GGCTCCAGCAGATCATCCAG-3' (*col5a1*). To assemble DNA templates for sgRNA transcription, gene-specific oligonucleotides containing the T7 promoter sequence (5'-TAATACGACTCACTATA-3'), the 20 base target site, and a complementary sequence were annealed to a constant oligonucleotide encoding the reverse-complement of the tracrRNA tail. sgRNAs were generated by in vitro transcription using the Megascript kit (Ambion). Cas9 mRNA was transcribed from linearized pCS2-Cas9 plasmid using the mMachine SP6 kit (Ambion). To generate mutants, one-cell stage wild-type embryos were injected with a mix containing the appropriate sgRNA at 20 ng/μl and Cas9 mRNA at 200 ng/μl. Injected fish were raised to adulthood and crossed to generate F1 embryos. T7 Endonuclease I assay (NEB) was then used to identify the presence of indel mutations in the targeted region of F1 fish. A *col1a2* allele containing 1 bp deletion ($col1a2^{ca108}$) and a *col5a1* allele with 4 bp deletion ($col5a1^{ca109}$) were identified (S6 Fig). For genotyping, small regions around the mutation sites were specifically amplified by PCR, which was followed by allele-specific restriction enzyme analysis. For $col1a2^{ca108}$, the primers used were 5'-TTTTAAAGACTCACATTTGCCTT-3' (forward) and 5'-CTCCGGGCTAGCTTTA-TATTTCGATT-3' (reverse). For $col5a1^{ca109}$, the primers used were 5'-ACTCTTGTTTGCTGTGCAGGT-3' (forward) and 5'-CTCACCGGTATTGGCCGTGTT-3' (reverse). Following PCR, the products were digested with a restriction enzyme which cuts only the wild type or the mutant allele. The enzymes used were BclI and BstCI (NEB) for *col1a2*^{ca108} and *col5a1*^{ca109}, respectively. The resulting band sizes were analyzed using gel electrophoresis. For *col1a2*^{ca108}, the BclI digest resulted in a single band of 473 bp in wild-type embryos, and two bands of 400 bp and 73 bp in homozygous *col1a2*$^{-/-}$ embryos. For *col5a1*^{ca109}, the BstCI digest resulted in multiple bands at 89, 44, 30, 18 and 9 bp in wild-type embryos, and bands of 107, 44, 30 and 9 bp in homozygous *col5a1*$^{-/-}$ embryos.

Plasmid injection

To visualize collagen distribution, we generated a *UAS*:*Col1a2-GFP* construct based on a previously published *pME-Col1a2-GFP* plasmid [52]. To generate the stable transgenic line, *UAS*:*Col1a2-GFP* (40 ng/μl) was co-injected with *tol2* transposase mRNA (40 ng/μl) into *col1a2*:*Gal4* embryos at the one-cell stage with 1 nl per embryo. Injected embryos were raised to adulthood and founders were identified based on GFP expression in F1 embryos. The *UAS*:*Col1a2-GFP* line was subsequently propagated in the absence of the Gal4 driver to prevent silencing of the transgene. For more mosaic labeling, *UAS*:*Col1a2-GFP* was injected at 10 ng/μl with *tol2* transposase mRNA. Injected embryos were screened for GFP expression at appropriate stages for imaging.

Morpholino injection

To inhibit ISV formation, morpholino oligonucleotides (Gene Tools, LLC) targeting the *etsrp* gene (*etsrp*^{MO}: 5'-CACTGAGTCCTTATTTCACTATATC-3') [77] were injected at 0.8 mM into one-cell stage embryos with 1.5 nl per embryo. Injected embryos were imaged at appropriate stages for the distribution of sclerotome derived cells.

In situ hybridization and immunohistochemistry

Whole-mount in situ hybridization and antibody staining were performed according to standard protocols. *col1a2* and *col5a1* antisense probes were used in this study. Double fluorescent in situ hybridization was performed using digoxigenin (DIG) and dinitrophenyl (DNP) labeled probes. For antibody labeling, the rabbit polyclonal antibody to GFP (1:500, MBL) was used. For fluorescent detection of antibody labeling, appropriate Alexa Fluor-conjugated secondary antibodies were used (1:500, Thermo Fisher).

Time-lapse imaging

Imaging was performed using the Olympus FV1200 confocal microscope as previously described [44]. Embryos older than 24 hpf were incubated in fish water with 1-phenyl 2-thiourea (PTU) to prevent pigmentation. Fish were anesthetized in 0.4% tricaine and mounted in 0.6% low melting point agarose. Z-stack images of the region of interest were then collected using the 20x objective at appropriate time intervals (5–15 mins) for up to 24 hours. Movies and images were processed using the Olympus Fluoview software and the Fiji software [78]. Cell tracing was performed manually using Fiji.

Cell ablation

To ablate perivascular fibroblasts, *nkx3.1*$^{NTR\text{-}mCherry}$ or *col1a2*$^{NTR\text{-}mCherry}$ embryos at desired developmental stages were treated with water (control group) or 5 mM metronidazole (MTZ, experimental group) for 24–48 hours. In some experiments, mCherry^{-} siblings treated with 5 mM MTZ in the same time windows were used as additional controls. Embryos were subsequently washed in fish water and imaged to confirm successful ablation of $mCherry^{+}$ cells.

Mechanical stress assay

To test the effect of physical stress on the vascular phenotype of collagen mutants, we adopted a mechanical overloading assay by raising embryos in a high-viscosity medium (0.6% methylcellulose) [56]. Heterozygotes for single mutants (*col1a2*$^{+/-}$ or *col5a1*$^{+/-}$) or double mutants (*col1a2*$^{+/-}$; *col5a1*$^{+/-}$) were intercrossed to obtain sibling embryos with different allele combinations. Resulting embryos were incubated in water (control group) or 0.6% methylcellulose (MC, experimental group) at 48 hpf. Fish were screened for hemorrhage in the trunk region approximately every 3 hours from 48 to 80 hpf and subsequently genotyped for *col1a2* and *col5a1*.

Quantification of single cell analysis

All measurements of single cell morphology were taken using the 'line selection' tool in Fiji. Cell length measurements were taken along the long axis of the cell, parallel to the neighboring ISV as shown in Fig 3E. Cell height measurements were taken at the midpoint of the cell body, orthogonal to the length measurement. Aspect ratio was calculated as cell length divided by cell height. Process lengths were measured by tracing along single processes using the 'segmented line' option under the line selection tool.

Quantification of blood vessel diameter variability

To quantify blood vessel diameters, we used the endothelial specific *kdrl*:*EGFP* reporter to fluorescently label intersegmental vessels. Embryos were imaged laterally in the trunk region (somite 12 to 18) and 8–10 ISVs were quantified per embryo. Using the 'line selection' tool in Fiji, four diameter measurements were taken for each ISV along its length and measurements were averaged to obtain mean vessel diameter. Standard deviation from the mean vessel diameter was plotted as a readout of ISV diameter variability. For dorsal aorta (DA) and posterior cardinal vein (PCV) measurements, diameter measurements were taken at 6–10 equidistant points along their length in the mid-trunk region with one measurement per somite. Mean vessel diameter and standard deviation from the mean were similarly graphed as ISV measurements.

Quantification of fluorescence intensity

To compare *pdgfrb*:*GFP* expression between pericytes and perivascular fibroblasts, GFP intensity measurements were taken using the 'oval selection' tool in Fiji. Circular regions of interest (ROIs) of 5.56 μm^2 area were drawn within individual cells and 'mean gray value' was measured. Five pericyte and perivascular fibroblast pairs were measured per embryo. For Col1a2-GFP measurements, a rectangular area of 500 by 160 pixels (393 μm x 126 μm) was drawn using the 'rectangular selection' tool in Fiji. The mean fluorescence intensity of the same region was measured before and after the water/MTZ treatment (GFP_{before} and GFP_{after}, respectively). The percentage change in Col1a2-GFP deposition was calculated using the following formula: (GFP_{after}—GFP_{before}) / GFP_{before} x 100%.

Statistical analysis

All graphs and statistical analysis were generated using the GraphPad PRISM software. Data were plotted with mean ± SEM indicated. Significance was calculated by performing using the non-parametric Mann-Whitney *U* test with two-tailed p values: $p > 0.05$ (ns, not significant), $p < 0.05$ (*), $p < 0.01$ (**), $p < 0.001$ (***) and $p < 0.0001$ (****).

Supporting information

S1 Fig. Characterization of collagen expression in perivascular fibroblasts. (A) Quantification of *col1a2*:*GFP* expression in perivascular fibroblasts in *nkx3.1*$^{NTR\text{-}mCherry}$; *col1a2*:*GFP* embryos at 52 hpf from Fig 1B. Total number of ISV associated mCherry$^+$ and GFP$^+$ cells were counted, and GFP$^+$mCherry$^+$ perivascular fibroblasts were graphed as a proportion of all mCherry$^+$ perivascular fibroblasts. Data are plotted as mean ± SEM. *n* = 17 embryos. (B) Co-expression of *col1a2* and *col5a1* in perivascular fibroblasts. *kdrl*:*EGFP* embryos at 48 hpf were co-labeled with *col1a2* (red) and *col5a1* (green) by double fluorescent in situ hybridization followed by immunofluorescence labeling using the GFP antibody (blue). Co-expression of *col1a2* and *col5a1* is observed in perivascular fibroblasts (arrowheads) along EGFP$^+$ ISVs. *n* = 23 embryos. Scale bar: 50 μm.
(TIF)

S2 Fig. Concurrent development of perivascular fibroblasts and the vasculature. (A) Developmental time-course of perivascular fibroblasts. *nkx3.1*$^{NTR\text{-}mCherry}$; *kdrl*:*EGFP* embryos were imaged at 26, 31, and 35 hpf to visualize different stages of perivascular fibroblast development. At 26 hpf, some *nkx3.1*$^{NTR\text{-}mCherry}$ cells (arrowhead) were visible along the ventral half of ISV sprouts. As ISV lumenization became visible (asterisk) at 31 hpf, more *nkx3.1*$^{NTR\text{-}mCherry}$ cells (arrowheads) appeared along ISVs. By 35 hpf, mCherry$^+$ cells (arrowheads) were present along the entire length of ISVs. (B) *nkx3.1*$^{NTR\text{-}mCherry}$; *kdrl*:*EGFP* embryos were injected with *etsrp* morpholino (*etsrp*^{MO}) at the one-cell stage to block blood vessel formation. Representative images of uninjected control embryos (top) and *etsrp*^{MO} injected morphants (bottom) at 48 hpf showing the distribution of sclerotome derived cells (red) in the presence and absence of ISVs (green), respectively. Trunk ISVs (asterisks) were visible in control embryos (top) but absent in morphants (bottom). Uninjected embryos had numerous mCherry$^+$ perivascular fibroblasts (arrowheads), while morphants showed many mCherry$^+$ sclerotome derived interstitial cells of unclear identity in the trunk (arrows). *n* = 15 (uninjected) and 23 (*etsrp*^{MO}) embryos. Scale bars: 50 μm.
(TIF)

S3 Fig. Characterization of transgenic reporters. (A) *pdgfrb*$^{NTR\text{-}mCherry}$; *pdgfrb*:*GFP* embryos imaged at 2 dpf (top) and 4 dpf (bottom). At 2 dpf, most perivascular fibroblasts were GFP$^+$mCherry$^-$ (white arrowheads) while a few cells were GFP$^+$mCherry$^+$ (cyan arrowheads). At 4 dpf, pericytes were GFP^{high}mCherry$^+$ (arrows), whereas perivascular fibroblasts were GFP^{low}mCherry$^-$ (arrowheads). *n* = 8 (2 dpf) and 7 (4 dpf) embryos. (B) *nkx3.1*$^{NTR\text{-}mCherry}$; *pdgfrb*:*GFP* embryos imaged at 2 dpf. Perivascular fibroblasts (arrowheads) were positive for both *nkx3.1*$^{NTR\text{-}mCherry}$ (red) and *pdgfrb*:*GFP* (green) reporters. *n* = 15 embryos. (C) Quantification of *pdgfrb*:*GFP* expression in pericytes and perivascular fibroblasts in *pdgfrb*$^{NTR\text{-}mCherry}$; *pdgfrb*:*GFP* embryos at 4 dpf from (A). GFP intensity was measured within individual GFP^{high}mCherry$^+$ pericytes and GFP^{low}mCherry$^-$ perivascular fibroblasts using ImageJ. Pericytes showed 2.5 fold increase in GFP intensity compared to perivascular fibroblasts at 4 dpf. Data are plotted as mean ± SEM. *n* = 35 pericytes and 35 perivascular fibroblasts from 7 embryos. Statistics: Mann-Whitney *U* test. Asterisk representation: p-value < 0.0001 (****). (D) Quantification of the mosaicism of *pdgfrb*$^{NTR\text{-}mCherry}$ compared to the *pdgfrb*:*GFP* line. Total mCherry$^+$ and GFP^{high} pericytes were counted in *pdgfrb*$^{NTR\text{-}mCherry}$; *pdgfrb*:*GFP* embryos at 4 dpf from (A), and double positive pericytes (GFP^{high}mCherry$^+$) were graphed as a

proportion of all GFP^{high} pericytes. On average, the *pdgfrb*$^{NTR\text{-}mCherry}$ transgene labeled 62% of GFP^{high} pericytes. Data are plotted as mean ± SEM. *n* = 7 embryos. (E) *col1a2*$^{NTR\text{-}mCherry}$*; col1a2*:*GFP* embryos imaged at 2 dpf. Due to the mosaic nature of both reporters, some perivascular fibroblasts were GFP^{+}mCherry^{+} (white arrowheads), some GFP^{+}mCherry^{-} (cyan arrowheads), and some GFP^{-}mCherry^{+} (yellow arrowheads). *n* = 5 embryos. Scale bars: 50 μm.
(TIF)

S4 Fig. Effect of early perivascular fibroblast ablation on major trunk vessels. To examine the impact of perivascular fibroblast ablation on large trunk vessels, *nkx3.1*$^{NTR\text{-}mCherry}$*; kdrl*:*EGFP* embryos were treated with either water or metronidazole (MTZ) from 38 to 62 hpf and then imaged as described in Fig 5A. Vessel diameters were measured at 6–10 points along each vessel using the line tool in ImageJ for both the dorsal aorta (DA) and the posterior cardinal vein (PCV). Mean diameter of each vessel and standard deviation from the mean (diameter variability) were plotted in (A-D). MTZ treated embryos showed reduced DA (A) and PCV (C) diameter and increased PCV diameter variability (D). DA diameter variability was not significantly different between MTZ treated and control embryos. *n* = 13 embryos (water); 9–14 embryos (MTZ). Results are graphed as mean ± SEM. Statistics: Mann-Whitney *U* test. Asterisk representation: p-value > 0.05 (ns, not significant); p-value < 0.01 (**); p-value < 0.001 (***).
(TIF)

S5 Fig. Late ablation of perivascular fibroblasts does not alter ISV morphology and minimally impacts collagen deposition. (A) Schematic of experimental procedure for late perivascular fibroblast ablation. *col1a2*$^{NTR\text{-}mCherry}$*; kdrl*:*EGFP* embryos were incubated in either water or MTZ from 4 to 5 dpf and imaged to visualize ISV morphology. (B) Representative images showing water (left) and MTZ (right) treated embryos. Water-treated control embryos had many mCherry^{+} cells (arrowheads), whereas MTZ treatment resulted in complete perivascular fibroblast ablation, with only mCherry^{+} debris visible (notched arrowheads). No distinguishable difference in ISV morphology was visible between MTZ treated and control embryos. (C) Quantification of ISV diameter variability in (B). ISV diameter and variability measurements were quantified as described in Fig 5. *n* = 103 ISVs from 9 embryos (water); 107 ISVs from 13 embryos (MTZ). (D) Schematic of experimental protocol to examine collagen deposition after perivascular fibroblast ablation between 4 and 5 dpf. *col1a2*:*Gal4; UAS*:*NTR-mCherry; UAS*:*Col1a2-GFP* embryos were incubated in water or metronidazole (MTZ) from 4–5 dpf. The same mid-trunk region of individual embryos was imaged prior to and after the drug treatment to visualize Col1a2-GFP deposition. (E) Representative images of water (left) and MTZ (right) treated embryos before and after the drug treatment. Water-treated control embryos showed many mCherry^{+} cells (arrowheads), while MTZ treatment resulted in complete ablation of mCherry^{+} cells with only mCherry^{+} debris (notched arrowhead) remaining. Control embryos showed a slight increase in Col1a2-GFP deposition around ISVs (arrows) from 4 to 5 dpf, while MTZ treated embryos showed largely similar levels of Col1a2-GFP during the same time period. (F) Quantification of changes in fluorescence intensity of Col1a2-GFP in (E). GFP intensity was measured for each embryo before and after the drug treatment and percentage change in GFP intensity was calculated using the following formula: $(GFP_{after}—GFP_{before}) / GFP_{before}$ x 100%. Control but not MTZ treated embryos showed a small increase in Col1a2-GFP deposition in the time period examined. *n* = 14 (water) and 13 (MTZ) embryos. Data are plotted as mean ± SEM. Statistics: Mann-Whitney *U* test. Asterisk representation: p-value > 0.05 (ns, not significant); p-value < 0.0001 (****). Scale bar: (B) 50 μm; (E) 25 μm.
(TIF)

S6 Fig. Generation of collagen mutants. (A) Sequencing chromatograms of *col1a2* WT and *col1a2*^{ca108} sequences. The sgRNA target sequence is underlined and the PAM motif is highlighted with a black box. The 1bp deletion in the *col1a2*^{ca108} sequence is denoted with an orange box. (B) Sequencing chromatograms of *col5a1* WT and *col5a1*^{ca109} sequences. The sgRNA target sequence is underlined and the PAM motif is highlighted with a black box. The 4bp deletion in the *col5a1*^{ca109} sequence is denoted with an orange box. (C) Alignment of *col1a2* WT and *col1a2*^{ca108} protein sequences. (D) Alignment of *col5a1* WT and *col5a1*^{ca109} protein sequences. Protein sequences were aligned using Clustal Omega (https://www.ebi.ac.uk/Tools/msa/clustalo/).
(TIF)

S7 Fig. Characterization of collagen mutants. (A) Distribution of genotypes in progeny of *col1a2*$^{+/-}$ intercrosses. Embryos from the mentioned crosses were grown and genotyped every 7 days from 7 dpf to 35 dpf to determine genotype distribution. Distribution of genotypes followed roughly Mendelian ratios at all stages examined. *n* = 24 (7 dpf), 16 (14 dpf), 24 (21 dpf), 25 (28 dpf), and 22 (35 dpf) fish. (B) Comparison of adult wild type and *col1a2*$^{-/-}$ siblings. (C) Distribution of genotypes in progeny of *col5a1*$^{+/-}$ intercrosses. Embryos from crosses of *col5a1*$^{+/-}$ adults were grown and genotyped at 3 day intervals from 5 dpf to 17 dpf. While the distribution of genotypes followed Mendelian ratios at 5 and 8 dpf, *col5a1*$^{-/-}$ fish were completely absent at 14 and 17 dpf. *n* = 39 (5 dpf), 55 (8 dpf), 43 (11 dpf), 36 (14 dpf), and 32 (17 dpf) fish. (D) Quantification of hemorrhage severity in collagen mutants shown in Fig 6D and 6E. Hemorrhage severity was scored by counting the number of visible hemorrhage foci present in the trunk. Fish with no visible hemorrhage were counted as 0. Increased physical stress in the viscous MC solution resulted in an increase in hemorrhage severity across mutants with different genotypes. *n* = 12 (*col1a2*$^{+/+}$*; col5a1*$^{-/-}$ + water); 11 (*col1a2*$^{+/+}$*; col5a1*$^{-/-}$ + MC); 20 (*col1a2*$^{+/-}$*; col5a1*$^{-/-}$ + water); 26 (*col1a2*$^{+/-}$*; col5a1*$^{-/-}$ + MC); 12 (*col1a2*$^{-/-}$*; col5a1*$^{-/-}$ + water); and 18 (*col1a2*$^{-/-}$*; col5a1*$^{-/-}$ + MC) embryos. Results were graphed as mean ± SEM. Statistics: Mann-Whitney *U* test. Asterisk representation: p-value $<$ 0.05 (*); p-value $<$ 0.0001 (****). Scale bar: (B) 2 mm.
(TIF)

S1 Video. Perivascular fibroblasts originate from the sclerotome. *nkx3.1*$^{NTR\text{-}mCherry}$*; kdrl*:*EGFP* embryos were imaged from 25 hpf to 49.5 hpf at ~8 minute intervals (7 min 58 sec) with time stamps indicated in the hh:mm format. Perivascular fibroblasts along ISVs were retrospectively traced to determine their cell of origin. One cell from the ventral sclerotome domain (cyan arrows) and one cell from sclerotome derived notochord associated cells (yellow arrows) were traced over 24.5 hours with their daughter cells indicated by the same colored arrows/arrowheads. Both sclerotome progenitors divided at least once to give rise to one perivascular fibroblast (arrowheads) as well as several interstitial cells (arrows). Snapshots of this time-lapse movie are shown in Fig 2B. *n* = 6 embryos. Scale bar: 50 μm.
(MP4)

S2 Video. Perivascular fibroblasts function as pericyte progenitors. *pdgfrb*$^{NTR\text{-}mCherry}$*; col1a2*:*GFP* embryos were imaged from 54 hpf to 73 hpf at 6 minute intervals with time stamps indicated in the hh:mm format. Newly differentiated pericytes were retrospectively traced to identify their cell of origin. One perivascular fibroblast (green, arrow) traced can be seen gradually upregulating *pdgfrb*$^{NTR\text{-}mCherry}$ expression and extending pericyte-like cellular processes (notched arrowhead). Snapshots of this time-lapse movie are shown in Fig 4A. *n* = 7 embryos. Scale bar: 25 μm.
(MP4)

S3 Video. Perivascular fibroblasts function as pericyte progenitors. *nkx3.1*$^{NTR\text{-}mCherry}$; *pdgfrb*:*GFP* embryos were imaged from 54 hpf to 76 hpf at 15 minute intervals with time stamps indicated in the hh:mm format. Two perivascular fibroblasts traced (arrows) can be seen gradually upregulating *pdgfrb*:*GFP* expression and extending pericyte-like cellular processes (notched arrowheads). Note that one of the traced cells (top arrows) migrated away from the ISV at 15:15. $n = 16$ embryos. Scale bar: 25 μm.
(MP4)

S1 Table. This table contains all the numerical data presented in this manuscript.
(XLSX)

Acknowledgments

We thank the zebrafish community for providing probes and reagents; Dr. Paul Martin for sharing the *pME-Col1a2-GFP* plasmid; Dr. Sarah Childs for sharing reagents, transgenic lines and providing critical input on this project; members of the Childs and Huang laboratories for discussions; and Dr. Paul Mains for critical comments on the manuscript.

Author Contributions

Conceptualization: Peng Huang.

Data curation: Arsheen M. Rajan, Roger C. Ma, Katrinka M. Kocha, Dan J. Zhang, Peng Huang.

Formal analysis: Arsheen M. Rajan, Roger C. Ma, Katrinka M. Kocha, Dan J. Zhang, Peng Huang.

Funding acquisition: Peng Huang.

Investigation: Arsheen M. Rajan, Roger C. Ma, Katrinka M. Kocha, Dan J. Zhang, Peng Huang.

Methodology: Arsheen M. Rajan, Roger C. Ma, Katrinka M. Kocha, Peng Huang.

Project administration: Peng Huang.

Resources: Peng Huang.

Software: Peng Huang.

Supervision: Peng Huang.

Validation: Arsheen M. Rajan, Peng Huang.

Visualization: Arsheen M. Rajan, Peng Huang.

Writing – original draft: Arsheen M. Rajan, Peng Huang.

Writing – review & editing: Arsheen M. Rajan, Roger C. Ma, Katrinka M. Kocha, Peng Huang.

References

1. Xu J, Shi G-P. Vascular wall extracellular matrix proteins and vascular diseases. Biochim Biophys Acta. 2014;(11):2106–19. https://doi.org/10.1016/j.bbadis.2014.07.008 PMID: 25045854
2. Murakami M, Simons M. Regulation of vascular integrity. Journal of Molecular Medicine. NIH Public Access; 2009; 87(6):571–82. https://doi.org/10.1007/s00109-009-0463-2 PMID: 19337719

3. Michel JB, Martin-Ventura JL, Egido J, Sakalihasan N, Treska V, Lindholt J, et al. Novel aspects of the pathogenesis of aneurysms of the abdominal aorta in humans. Cardiovasc Res. 2011; 90(1):18–27. https://doi.org/10.1093/cvr/cvq337 PMID: 21037321
4. Sakalihasan N, Michel JB, Katsargyris A, Kuivaniemi H, Defraigne JO, Nchimi A, et al. Abdominal aortic aneurysms. Nature Reviews Disease Primers. 2018; 4:34. https://doi.org/10.1038/s41572-018-0030-7 PMID: 30337540
5. Qureshi AI, Mendelow AD, Hanley DF. Intracerebral haemorrhage. The Lancet. 2009; 373:1632–44. https://doi.org/10.1016/S0140-6736(09)60371-8 PMID: 19427958
6. Brisman JL, Song JK, Newell DW. Cerebral aneurysms. The New England Journal of Medicine. 2006; 355(9):928–39. https://doi.org/10.1056/NEJMra052760 PMID: 16943405
7. Dejana E, Tournier-Lasserve E, Weinstein BM. The Control of Vascular Integrity by Endothelial Cell Junctions: Molecular Basis and Pathological Implications. Dev Cell. 2009 Feb 17; 16(2):209–21. https://doi.org/10.1016/j.devcel.2009.01.004 PMID: 19217423
8. Gaengel K, Genové G, Armulik A, Betsholtz C. Endothelial-mural cell signaling in vascular development and angiogenesis. Arterioscler Thromb Vasc Biol. 2009 May 1; 29(5):630–8. https://doi.org/10.1161/ATVBAHA.107.161521 PMID: 19164813
9. Levéen P, Pekny M, Gebre-Medhin S, Swolin B, Larsson E, Betsholtz C. Mice deficient for PDGF B show renal, cardiovascular, and hematological abnormalities. Genes Dev. 1994; 8(16):1875–87. https://doi.org/10.1101/gad.8.16.1875 PMID: 7958863
10. Lindahl P, Johansson BR, Levéen P, Betsholtz C. Pericyte loss and microaneurysm formation in PDGF-B-deficient mice. Science. 1997 Jul 11; 277(5323):242–5. https://doi.org/10.1126/science.277.5323.242 PMID: 9211853
11. Soriano P. Abnormal kidney development and hematological disorders in PDGF β- receptor mutant mice. Genes Dev. 1994; 8(16):1888–96. https://doi.org/10.1101/gad.8.16.1888 PMID: 7958864
12. Hellström M, Gerhardt H, Kalén M, Li X, Eriksson U, Wolburg H, et al. Lack of pericytes leads to endothelial hyperplasia and abnormal vascular morphogenesis. J Cell Biol. 2001 Feb 5; 152(3):543–53. https://doi.org/10.1083/jcb.153.3.543 PMID: 11331305
13. Bjarnegård M, Enge M, Norlin J, Gustafsdottir S, Fredriksson S, Abramsson A, et al. Endothelium-specific ablation of PDGFB leads to pericyte loss and glomerular, cardiac and placental abnormalities. Development. 2004 Apr; 131(8):1847–57. https://doi.org/10.1242/dev.01080 PMID: 15084468
14. Rhodes JM, Simons M. The extracellular matrix and blood vessel formation: Not just a scaffold: Angiogenesis Review Series. J Cell Mol Med. 2007 Mar; 11(2):176–205. https://doi.org/10.1111/j.1582-4934.2007.00031.x PMID: 17488472
15. Löhler J, Timpl R, Jaenisch R. Embryonic lethal mutation in mouse collagen I gene causes rupture of blood vessels and is associated with erythropoietic and mesenchymal cell death. Cell. 1984 Sep 1; 38(2):597–607. https://doi.org/10.1016/0092-8674(84)90514-2 PMID: 6467375
16. Liu X, Wu H, Byrne M, Krane S, Jaenisch R. Type III collagen is crucial for collagen I fibrillogenesis and for normal cardiovascular development. Proc Natl Acad Sci. 1997 Mar 4; 94(5):1852–6. https://doi.org/10.1073/pnas.94.5.1852 PMID: 9050868
17. Pöschl E, Schlötzer-Schrehardt U, Brachvogel B, Saito K, Ninomiya Y, Mayer U. Collagen IV is essential for basement membrane stability but dispensable for initiation of its assembly during early development. Development. 2004 Apr; 131(7):1619–28. https://doi.org/10.1242/dev.01037 PMID: 14998921
18. Thyboll J, Kortesmaa J, Cao R, Soininen R, Wang L, Iivanainen A, et al. Deletion of the Laminin 4 Chain Leads to Impaired Microvessel Maturation. Mol Cell Biol. 2002 Feb 15; 22(4):1194–202. https://doi.org/10.1128/mcb.22.4.1194-1202.2002 PMID: 11809810
19. Malfait F. Vascular aspects of the Ehlers-Danlos Syndromes. Matrix Biol. 2018; 71–72:380–395. https://doi.org/10.1016/j.matbio.2018.04.013 PMID: 29709596
20. Yamazaki T, Mukouyama Y. Tissue Specific Origin, Development, and Pathological Perspectives of Pericytes. Front Cardiovasc Med. 2018; 5:78. https://doi.org/10.3389/fcvm.2018.00078 PMID: 29998128
21. Holm A, Heumann T, Augustin HG. Microvascular Mural Cell Organotypic Heterogeneity and Functional Plasticity. Trends in Cell Biology. 2018; 28(4): 302–316. https://doi.org/10.1016/j.tcb.2017.12.002 PMID: 29307447
22. Armulik A, Genové G, Betsholtz C. Pericytes: Developmental, Physiological, and Pathological Perspectives, Problems, and Promises. Dev Cell. 2011; 21(2):193–215. https://doi.org/10.1016/j.devcel.2011.07.001 PMID: 21839917
23. Majesky MW. Developmental basis of vascular smooth muscle diversity. Arterioscler Thromb Vasc Biol. 2007 Jun; 27(6):1248–58. https://doi.org/10.1161/ATVBAHA.107.141069 PMID: 17379839

24. Crisan M, Corselli M, Chen WCW, Péault B. Perivascular cells for regenerative medicine. J Cell Mol Med. 2012 Dec; 16(12):2851–60. https://doi.org/10.1111/j.1582-4934.2012.01617.x PMID: 22882758

25. Soderblom C, Luo X, Blumenthal E, Bray E, Lyapichev K, Ramos J, et al. Perivascular fibroblasts form the fibrotic scar after contusive spinal cord injury. J Neurosci. 2013; 33(34):13882–7. https://doi.org/10.1523/JNEUROSCI.2524-13.2013 PMID: 23966707

26. Guillemin GJ, Brew BJ. Microglia, macrophages, perivascular macrophages, and pericytes: a review of function and identification. J Leukoc Biol. 2004 Mar 1; 75(3):388–97. https://doi.org/10.1189/jlb.0303114 PMID: 14612429

27. Macvicar BA, Newman EA. Astrocyte regulation of blood flow in the brain. Cold Spring Harb Perspect Biol. 2015; 7(5):1–15.

28. Marques S, Zeisel A, Codeluppi S, Van Bruggen D, Falcão AM, Xiao L, et al. Oligodendrocyte heterogeneity in the mouse juvenile and adult central nervous system. Science (80-). 2016 Jun 10; 352 (6291):1326–9. https://doi.org/10.1126/science.aaf6463 PMID: 27284195

29. Zeisel A, Hochgerner H, Lönnerberg P, Johnsson A, Memic F, van der Zwan J, et al. Molecular Architecture of the Mouse Nervous System. Cell. 2018 Aug 9; 174(4):999–1014.e22. https://doi.org/10.1016/j.cell.2018.06.021 PMID: 30096314

30. Saunders A, Macosko EZ, Wysoker A, Goldman M, Krienen FM, de Rivera H, et al. Molecular Diversity and Specializations among the Cells of the Adult Mouse Brain. Cell. 2018 Aug 9; 174(4):1015–1030.e16. https://doi.org/10.1016/j.cell.2018.07.028 PMID: 30096299

31. Vanlandewijck M, He L, Mäe MA, Andrae J, Ando K, Del Gaudio F, et al. A molecular atlas of cell types and zonation in the brain vasculature. Nature. 2018 Feb 14; 554(7693):475–80. https://doi.org/10.1038/nature25739 PMID: 29443965

32. Kelly KK, MacPherson AM, Grewal H, Strnad F, Jones JW, Yu J, et al. Col1a1+ perivascular cells in the brain are a source of retinoic acid following stroke. BMC Neurosci. 2016; 17(1):49. https://doi.org/10.1186/s12868-016-0284-5 PMID: 27422020

33. Fernández-Klett F, Potas JR, Hilpert D, Blazej K, Radke J, Huck J, et al. Early loss of pericytes and perivascular stromal cell-induced scar formation after stroke. J Cereb Blood Flow Metab. 2013 Mar; 33 (3):428–39. https://doi.org/10.1038/jcbfm.2012.187 PMID: 23250106

34. Göritz C, Dias DO, Tomilin N, Barbacid M, Shupliakov O, Frisén J. A pericyte origin of spinal cord scar tissue. Science. 2011 Jul 8; 333(6039):238–42. https://doi.org/10.1126/science.1203165 PMID: 21737741

35. Makihara N, Arimura K, Ago T, Tachibana M, Nishimura A, Nakamura K, et al. Involvement of platelet-derived growth factor receptor β in fibrosis through extracellular matrix protein production after ischemic stroke. Exp Neurol. 2015 Feb 1; 264:127–34. https://doi.org/10.1016/j.expneurol.2014.12.007 PMID: 25510317

36. Gore A V., Monzo K, Cha YR, Pan W, Weinstein BM. Vascular development in the zebrafish. Cold Spring Harb Perspect Med. 2012 May 1; 2(5):a006684. https://doi.org/10.1101/cshperspect.a006684 PMID: 22553495

37. Howe K, Clark MD, Torroja CF, Torrance J, Berthelot C, Muffato M, et al. The zebrafish reference genome sequence and its relationship to the human genome. Nature. 2013 Apr 25; 496(7446):498–503. https://doi.org/10.1038/nature12111 PMID: 23594743

38. Chico TJA, Ingham PW, Crossman DC. Modeling Cardiovascular Disease in the Zebrafish. Trends Cardiovasc Med. 2008 May; 18(4):150–5. https://doi.org/10.1016/j.tcm.2008.04.002 PMID: 18555188

39. Isogai S, Horiguchi M, Weinstein BM. The vascular anatomy of the developing zebrafish: An atlas of embryonic and early larval development. Dev Biol. 2001 Feb 15; 230(2):278–301. https://doi.org/10.1006/dbio.2000.9995 PMID: 11161578

40. Santoro MM, Pesce G, Stainier DY. Characterization of vascular mural cells during zebrafish development. Mech Dev. 2009 Aug; 126(8–9):638–49. https://doi.org/10.1016/j.mod.2009.06.1080 PMID: 19539756

41. Bahrami N, Childs SJ. Pericyte biology in zebrafish. In: Advances in Experimental Medicine and Biology. Springer New York LLC; 2018. p. 33–51.

42. Isogai S, Lawson ND, Torrealday S, Horiguchi M, Weinstein BM. Angiogenic network formation in the developing vertebrate trunk. Development. 2003 Nov 1; 130(21):5281–90. https://doi.org/10.1242/dev.00733 PMID: 12954720

43. Ando K, Fukuhara S, Izumi N, Nakajima H, Fukui H, Kelsh RN, et al. Clarification of mural cell coverage of vascular endothelial cells by live imaging of zebrafish. Development. 2016 Apr 15; 143(8):1328–39. https://doi.org/10.1242/dev.132654 PMID: 26952986

44. Ma RC, Jacobs CT, Sharma P, Kocha KM, Huang P. Stereotypic generation of axial tenocytes from bipartite sclerotome domains in zebrafish. Moens C, editor. PLOS Genet. 2018 Nov 2; 14(11): e1007775. https://doi.org/10.1371/journal.pgen.1007775 PMID: 30388110

45. Olson LE, Soriano P. PDGFRβ signaling regulates mural cell plasticity and inhibits fat development. Dev Cell. 2011 Jun 14; 20(6):815–26. https://doi.org/10.1016/j.devcel.2011.04.019 PMID: 21664579

46. Hellström M, Kalen M, Lindahl P, Abramsson A, Betsholtz C. Role of PDGF-B and PDGFR-β in recruitment of vascular smooth muscle cells and pericytes during embryonic blood vessel formation in the mouse. Development. 1999;(126):3047–55. PMID: 10375497

47. Bahrami N, Childs SJ. Development of vascular regulation in the zebrafish embryo. Dev. 2020 May 1; 147: dev183061. https://doi.org/10.1242/dev.183061 PMID: 32423977

48. Whitesell TR, Chrystal PW, Ryu JR, Munsie N, Grosse A, French CR, et al. foxc1 is required for embryonic head vascular smooth muscle differentiation in zebrafish. Dev Biol. 2019 Sep 1; 453(1):34–47. https://doi.org/10.1016/j.ydbio.2019.06.005 PMID: 31199900

49. Stratman AN, Pezoa SA, Farrelly OM, Castranova D, Dye LE, Butler MG, et al. Interactions between mural cells and endothelial cells stabilize the developing zebrafish dorsal aorta. Dev. 2017 Jan 1; 144 (1):115–27. https://doi.org/10.1242/dev.143131 PMID: 27913637

50. Sharma P, Ruel TD, Kocha KM, Liao S, Huang P. Single cell dynamics of embryonic muscle progenitor cells in zebrafish. Dev. 2019 Jul 1; 146(14):dev178400. https://doi.org/10.1242/dev.178400 PMID: 31253635

51. Curado S, Stainier DYR, Anderson RM. Nitroreductase-mediated cell/tissue ablation in zebrafish: A spatially and temporally controlled ablation method with applications in developmental and regeneration studies. Nat Protoc. 2008 May; 3(6):948–54. https://doi.org/10.1038/nprot.2008.58 PMID: 18536643

52. Morris JL, Cross SJ, Lu Y, Kadler KE, Lu Y, Dallas SL, et al. Live imaging of collagen deposition during skin development and repair in a collagen I—GFP fusion transgenic zebrafish line. Dev Biol. 2018; 441 (1):4–11. https://doi.org/10.1016/j.ydbio.2018.06.001 PMID: 29883658

53. Gagnon JA, Valen E, Thyme SB, Huang P, Ahkmetova L, Pauli A, et al. Efficient Mutagenesis by Cas9 Protein-Mediated Oligonucleotide Insertion and Large-Scale Assessment of Single-Guide RNAs. PLoS One. 2014 May 29; 9(5): e98186. https://doi.org/10.1371/journal.pone.0098186 PMID: 24873830

54. Fisher S, Jagadeeswaran P, Halpern ME. Radiographic analysis of zebrafish skeletal defects. Dev Biol. 2003 Dec 1; 264(1):64–76. https://doi.org/10.1016/s0012-1606(03)00399-3 PMID: 14623232

55. Gistelinck C, Kwon RY, Malfait F, Symoens S, Harris MP, Henke K, et al. Zebrafish type I collagen mutants faithfully recapitulate human type I collagenopathies. Proc Natl Acad Sci. 2018 Aug 21; 115 (34):E8037–46. https://doi.org/10.1073/pnas.1722200115 PMID: 30082390

56. Hall TE, Bryson-Richardson RJ, Berger S, Jacoby AS, Cole NJ, Hollway GE, et al. The zebrafish candyfloss mutant implicates extracellular matrix adhesion failure in laminin α2-deficient congenital muscular dystrophy. Proc Natl Acad Sci. 2007 Apr 24; 104(17):7092–7. https://doi.org/10.1073/pnas.0700942104 PMID: 17438294

57. He L, Vanlandewijck M, Mäe MA, Andrae J, Ando K, Gaudio F Del, et al. Single-cell RNA sequencing of mouse brain and lung vascular and vessel-associated cell types. Sci Data. 2018 Aug 21; 5:180160. https://doi.org/10.1038/sdata.2018.160 PMID: 30129931

58. Ando K, Wang W, Peng D, Chiba A, Lagendijk AK, Barske L, et al. Peri-arterial specification of vascular mural cells from naïve mesenchyme requires notch signaling. Dev. 2019; 146: dev165589. https://doi.org/10.1242/dev.165589 PMID: 30642834

59. Etchevers HC, Vincent C, Le Douarin NM, Couly GF. The cephalic neural crest provides pericytes and smooth muscle cells to all blood vessels of the face and forebrain. Development. 2001; 128(7):1059–68. PMID: 11245571

60. Bergwerff M, Verberne ME, DeRuiter MC, Poelmann RE, Gittenberger-de Groot AC. Neural crest cell contribution to the developing circulatory system implications for vascular morphology? Circ Res. 1998 Feb 9; 82(2):221–31. https://doi.org/10.1161/01.res.82.2.221 PMID: 9468193

61. Wang Y, Pan L, Moens CB., Appel B. Notch3 establishes brain vascular integrity by regulating pericyte number. Dev. 2014; 141: 307–17. https://doi.org/10.1242/dev.096107 PMID: 24306108

62. Domenga V, Fardoux P, Lacombe P, Monet M, Maciazek J, Krebs LT, et al. Notch3 is required for arterial identity and maturation of vascular smooth muscle cells. Genes Dev. 2004 Nov 15; 18(22):2730–5. https://doi.org/10.1101/gad.308904 PMID: 15545631

63. Liu H, Zhang W, Kennard S, Caldwell RB, Lilly B. Notch3 is critical for proper angiogenesis and mural cell investment. Circ Res. 2010 Oct 1; 107(7):860–70. https://doi.org/10.1161/CIRCRESAHA.110.218271 PMID: 20689064

64. Kofler NM, Cuervo H, Uh MK, Murtomäki A, Kitajewski J. Combined deficiency of Notch1 and Notch3 causes pericyte dysfunction, models CADASIL, and results in arteriovenous malformations. Sci Rep. 2015; 5(June):1–13.

65. Ton Q V, Leino D, Mowery SA, Bredemeier NO, Lafontant PJ, Lubert A, et al. Collagen COL22A1 maintains vascular stability and mutations in COL22A1 are potentially associated with intracranial aneurysms. Disease Models and Mechanisms. 2018; 11:dmm033654. https://doi.org/10.1242/dmm.033654 PMID: 30541770

66. Ricard-Blum S. The Collagen Family. Cold Spring Harb Perspect Biol. 2011; 3(1):1–19. https://doi.org/10.1101/cshperspect.a004978 PMID: 21421911

67. Mak KM, Png CYM, Lee DJ. Type V Collagen in Health, Disease, and Fibrosis. Anat Rec. 2016; 299 (5):613–29.

68. Bretaud S, Nauroy P, Malbouyres M, Ruggiero F. Fishing for collagen function: About development, regeneration and disease. Semin Cell Dev Biol. 2019 May 1; 89:100–8. https://doi.org/10.1016/j.semcdb.2018.10.002 PMID: 30312775

69. De Paepe A, Malfait F. Bleeding and bruising in patients with Ehlers-Danlos syndrome and other collagen vascular disorders. Br J Haematol; 2004; 127:491–500. https://doi.org/10.1111/j.1365-2141.2004.05220.x PMID: 15566352

70. Aszódi A, Legate KR, Nakchbandi I, Fässler R. What Mouse Mutants Teach Us About Extracellular Matrix Function. Annu Rev Cell Dev Biol. 2006 Nov; 22(1):591–621. https://doi.org/10.1146/annurev.cellbio.22.010305.104258 PMID: 16824013

71. Wenstrup RJ, Florer JB, Brunskill EW, Bell SM, Chervoneva I, Birk DE. Type V collagen controls the initiation of collagen fibril assembly. J Biol Chem. 2004 Dec 17; 279(51): 53331–7. https://doi.org/10.1074/jbc.M409622200 PMID: 15383546

72. Dias DO, Kim H, Holl D, Werne Solnestam B, Lundeberg J, Carlén M, et al. Reducing Pericyte-Derived Scarring Promotes Recovery after Spinal Cord Injury. Cell. 2018; 173(1):153–165.e22. https://doi.org/10.1016/j.cell.2018.02.004 PMID: 29502968

73. Choi J, Dong L, Ahn J, Dao D, Hammerschmidt M, Chen JN. FoxH1 negatively modulates flk1 gene expression and vascular formation in zebrafish. Dev Biol. 2007 Apr 15; 304(2):735–44. https://doi.org/10.1016/j.ydbio.2007.01.023 PMID: 17306248

74. Proulx K, Lu A, Sumanas S. Cranial vasculature in zebrafish forms by angioblast cluster-derived angiogenesis. Dev Biol. 2010 Dec 1; 348(1):34–46. https://doi.org/10.1016/j.ydbio.2010.08.036 PMID: 20832394

75. Davison JM, Akitake CM, Goll MG, Rhee JM, Gosse N, Baier H, et al. Transactivation from Gal4-VP16 transgenic insertions for tissue-specific cell labeling and ablation in zebrafish. Dev Biol. 2007 Apr 15; 304(2):811–24. https://doi.org/10.1016/j.ydbio.2007.01.033 PMID: 17335798

76. Montague TG, Cruz JM, Gagnon JA, Church GM, Valen E. CHOPCHOP: A CRISPR/Cas9 and TALEN web tool for genome editing. Nucleic Acids Res. 2014 Jul 1; 42:W401–7. https://doi.org/10.1093/nar/gku410 PMID: 24861617

77. Sumanas S, Lin S. Ets1-related protein is a key regulator of vasculogenesis in zebrafish. PLoS Biol. 2006; 4(1): e10. https://doi.org/10.1371/journal.pbio.0040010 PMID: 16336046

78. Schindelin J, Arganda-Carreras I, Frise E, Kaynig V, Longair M, Pietzsch T, et al. Fiji: An open-source platform for biological-image analysis. Nature Methods. 2012; 9: 676–82. https://doi.org/10.1038/nmeth.2019 PMID: 22743772